Pietrosanti D, De Angelis M and Giaralis A. (2020) Experimental study and numerical modeling of nonlinear dynamic response of SDOF system equipped with tuned mass damper inerter (TMDI) tested on shaking table under harmonic excitation, *International Journal of Mechanical Sciences*, 184, 105762.

Experimental study and numerical modeling of nonlinear dynamic response of SDOF system equipped with tuned mass damper inerter (TMDI) tested on shaking table under harmonic excitation

Daniele Pietrosanti[a], Maurizio De Angelis[a*], Agathoklis Giaralis[b]

[a] Department of Structural and Geotechnical Engineering, Sapienza University of Rome, Rome, IT

[b] Department of Civil Engineering, City, University of London, London, UK

[*] Corresponding author: *maurizio.deangelis@uniroma1.it*, +39 0644585109, +39 0644585292

Abstract

This paper considers a novel shaking table testing campaign to assess the tuned mass-damper-inerter (TMDI) vibrations suppression attributes in harmonically excited structures under the combined effect of nonlinear structural response and inerter device behavior deviating from the ideal linear inerter element developing acceleration-dependent force proportional to the inertance constant. Physical specimens of TMDI-equipped single-degree-of-freedom (SDOF) structure featuring a custom-built rack-and-pinion flywheel inerter device to connect the TMDI secondary mass to the ground are considered. Damping and elastic properties are endowed to the SDOF structure and to the TMDI via high damping rubber bearings (HDRBs) exhibiting softening nonlinear elastic behaviour. Comprehensive experimental data in time and frequency domains are presented for 9 specimens with different sets of secondary mass and inertance subject to sine-sweep excitations for three different amplitudes. The data demonstrate that the main practical advantage of the TMDI established in the literature for linear structures and ideal inerters (i.e., improved vibration suppression through increasing inertance without increasing secondary mass leading to lightweight vibration absorbers) is maintained for nonlinear structures and inerter devices. Moreover, a comparison of experimental data

with data derived from two different nonlinear parametric numerical models capturing faithfully the HDRBs response, one using a nonlinear mechanical model to represent the inerter device and the other using an ideal linear inerter element instead, demonstrate that displacement, acceleration and base shear response of the SDOF structure is insignificantly influenced by the deviation of the inerter device from the ideal inerter element. This outcome paves the way for developing simplified, thus practically meritorious, optimal TMDI tuning approaches adopting the ideal inerter element assumption to model physical inerter devices.

Keywords: Inerter; Tuned Mass Damper Inerter; shaking table testing; experimental parametric analysis; experimental and numerical nonlinear dynamic response; high damping rubber bearings

1. Introduction

Passive vibration suppression in dynamically excited structural systems is usually achieved by employing one, or a combination, of the following three types of devices: dampers, vibration isolators, and dynamic vibration absorbers (e.g., [1]). Dampers are installed within structures and dissipate kinetic energy through viscous behavior (e.g., fluid dampers developing velocity-dependent forces), viscoelastic behavior (e.g., elastomeric dampers developing velocity-and-displacement-dependent forces), or friction mechanisms (e.g., metallic dampers) [2]. Vibration isolators are mostly elastomeric [3] or sliding [4] bearings placed in between the structure and its foundation/support. This consideration leads to base isolated structures with elongated fundamental natural period which minimizes the likelihood of resonance with excitation frequencies. Additionally, high damping rubber bearings (HDRBs) provide supplemental damping to base isolated structures acting similarly to dampers. Dynamic vibration absorbers, with main representative the tuned mass damper (TMD), consisted of a secondary oscillatory mass attached to the main (structures) structure through dampers

and stiffeners [5]. The damping and stiffness properties of TMDs are tuned to a particular (target) structural natural frequency such that kinetic energy is transferred from the main structure to the secondary mass through resonance and eventually dissipated by the dampers [6], while multiple TMDs diffused in structures can further achieve multi-modal vibration suppression effect [7].

In recent years, inerter-based passive vibration suppression configurations emerged [8-10], the most widely considered being the tuned viscous mass damper (TVMD) [11], the tuned inerter damper (TID) [12] and the tuned mass damper inerter (TMDI) [13], by coupling dampers and TMDs with an *inerter*. The latter is a device developing acceleration-dependent force proportional to a constant termed *inertance* and assuming mass units [14]. Pertinent theoretical studies established that these configurations achieve secondary attached mass reduction and/or improved vibration control efficiency in fixed-based (e.g., [15-25]) as well as in base isolated structural systems (e.g., [26-30]). Moreover, theoretical work by Basili et al. [31-33] demonstrated the effectiveness of linking adjacent structural systems through inerter-based connections to improve their performance to dynamic loads. All the above theoretical studies rely largely on the assumptions that (I) inertance can scale-up independently of the physical mass of inerter devices and (II) the inerter behaves as an ideal linear mechanical element as defined by Smith [14]. Assumption (I) is realistic to a large extent. Indeed, solid inerter devices accomplishing inertance values several orders larger than their mass have been devised and experimentally verified by relying on transforming, through gearing, input translational motion into rotational motion of a flywheel (i.e., a lightweight fast-spinning disk) using rack-and-pinion (e.g., [34-36]) or ball-screw mechanisms (e.g., [37-40]). Moreover, favourable inertance scalability attribute has been exhibited by inerters relying on fluid circulating within a helical tube (fluid inerters) [41-43], or driving a flywheel through a hydraulic motor (hydraulic inerters) [44-45]. However, assumption (II) is less realistic since experimental dynamic testing to standalone physical prototypes of inerter devices demonstrate deviation from the ideal inerter behavior due to various

effects dependent on the specifications, operational frequency range, and technology used to implement the inerter (i.e., mechanical, hydraulic or fluid).

In this regard, the issue of assessing the influence of physical inerter devices deviating from the ideal inerter element behaviour to the vibration suppression potential of inerter-based configurations and, more generally, to the dynamic behaviour of structural systems received lately some attention. Some research work along these lines has been numerical/computational undertaken in two steps (e.g., [46-47]): First, inerter behaviour is analytically expressed by parametric force-deformation relationships fitted into experimental data derived from dynamic testing of physical device prototypes. Then, these relationships are incorporated into equations of motion of the total structural system and solved (integrated) numerically for specific excitations. Such approaches, though, cannot capture potential interaction effects of the inerter devices with structures as well as inertance scaling effects. This issue is addressed by fully experimental approaches. Among these, Nakamura et al. [39] conducted shaking table tests of a linear three-storey shear frame equipped with inerter-enhanced electromagnetic dampers. More recently, Gonzales-Buelga et al. [48] considered real-time dynamic hybrid testing (substructuring) to study the effectiveness of the TID for vibration suppression of a SDOF structure featuring a commercial inerter device targeting vehicle suspension applications. With the exception of the inerter device, the TID and the SDOF oscillator were computer/numerically simulated assuming linear behaviour. Further, Brezksi et al. [36] developed a flywheel-based inerter utilizing a rack and pinion mechanism along with continuously varying transmission to vary inertance and tested it experimentally in a rig that modelled a linear SDOF system with parallel spring, damper and inerter.

Notably, to date, all research studies on inerter-based vibration control using physical inerter devices considered overall linear structural behaviour. Still, in several applications, notwithstanding earthquake engineering, structures as well as absorbers may behave in a nonlinear fashion. To the best of the authors knowledge, the response of nonlinear structures equipped with inerter-based

vibration suppression devices has not been studied thus far experimentally. This paper takes a first step towards this aim, by examining through shaking table testing the behavior of TMDIs with grounded inerter and different inertial properties attached to a base-excited SDOF structure in which the structure as well as the TMDI behave in nonlinear elastic fashion. A rack-and-pinion flywheel-based inerter prototype is used in the herein considered experimental specimens (physical models) while elastic and damping properties of the TMDI and of the SDOF structure are implemented via elastomeric isolators exhibiting nonlinear elastic behavior. Harmonic excitation with varying frequencies within a wide range of interest to civil engineering applications is applied and with various intensities.

The remainder of the paper is organized as follows. In Section 2, the physical models, the shaking table setup, and the instrumentation used in the testing are described. Section 3 reports and discusses comprehensive experimental data focusing on the influence of excitation frequency and amplitude to structural response in time and in frequency domain as well as on the influence of different TMDI inertial properties (i.e., secondary mass and inertance) to the overall response of the physical specimens. Section 4 fits experimental data to a parametric nonlinear model aiming to capture and characterize the exhibited nonlinear structural behavior. Finally, section 5 summarizes concluding remarks.

2. Physical modelling, shaking table setup and instrumentation

2.1. Theoretical Model

Consider the linear lumped-mass two degree-of-freedom (2-DOF) dynamical system shown in Figure 1(a). It consists of three components: (i) a main mass, m_I, connected to the ground through a visco-elastic link with stiffness property k_I and damping property c_I, (ii) a secondary mass, m_T,

connected to the main mass through a visco-elastic link with stiffness property k_T and damping property c_T, and (iii) an ideal inerter mechanical element linking the secondary mass to the ground. The first component is the primary structure (PS) which may be interpreted either as a damped structure modelled as single degree-of-freedom (SDOF) oscillator or as a base-isolated structure with very stiff superstructure taken as a perfectly rigid body. The second component is the standard linear TMD (e.g., [6]). The third component is a mechanical element resisting relative acceleration of its two ends through the inertance, *b*, proportionality constant [14]. The combination of the TMD with a grounded inerter, i.e., components (ii) and (iii), is termed TMDI, introduced by Marian and Giaralis [13] and subsequently studied by the authors [17, 49], to enhance TMD vibration suppression efficiency by increasing the inertia of the TMD without adding gravitational mass. This is because a grounded inerter element acts as a weightless mass with inertia *b* [14], therefore, decoupling the gravitational from the inertial mass. The dynamic response of undamped SDOF structures with grounded TMDIs has been analytically investigated for random and harmonic base excitations in [13] and [49], respectively. Further, the response of grounded TMDI-equipped damped SDOF structures to earthquake excitations has been numerically assessed by Pietrosanti et al. [17]. Moreover, the potential of the grounded TMDI to suppress excessive seismic demands in base isolated structures has been studied by De Domenico and Ricciardi [28] and De Angelis et al. [30] for the case of linear isolators and by De Domenico and Ricciardi [29] for the case of nonlinear isolators. Herein, the response of the 2-DOF dynamical system in Figure 1(a) to ground excitation is studied experimentally. To this aim, a series of physical models approximating the properties of the considered system shown pictorially in Figure 1(b) are built on a shaking table as detailed in the two following sub-sections.

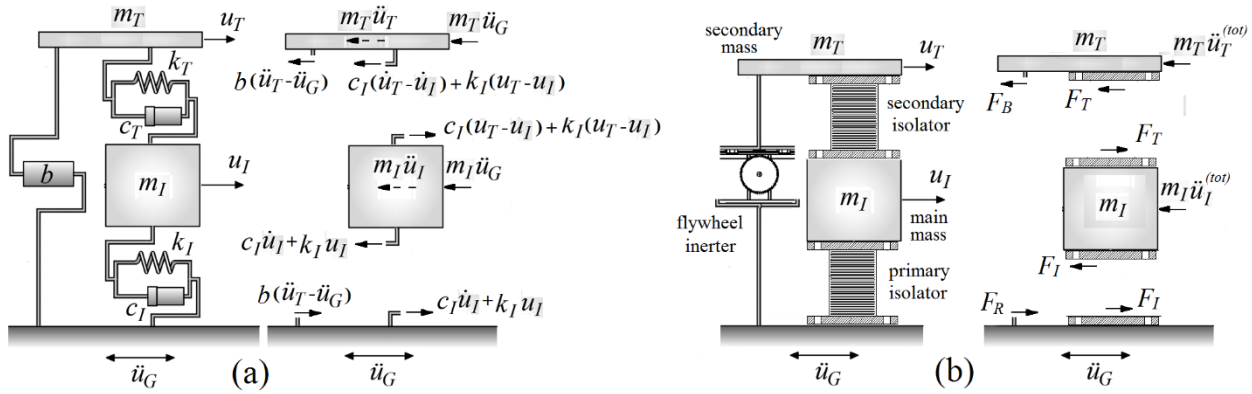

Figure 1. Idealized lumped-mass model of SDOF primary structure with attached tuned mass damper inerter (TMDI) and free body diagram. (a) Linear theoretical system, (b) Physical model.

2.2. Physical models description

The 2-DOF system of Figure 1(a) is approximated by physical models (specimens) schematically shown in Figure 1(b). Side and aerial view photos of a sample specimen mounted on the shaking table is shown in Figure 2. In the considered specimens, two HDRB isolators are used in place of the visco-elastic links while a custom-made flywheel-based inerter device is used in place of the ideal inerter element. The specimens have common primary mass and isolators, but different inertial properties: secondary mass and inertance. The reason for parametrizing the secondary mass in the experimental campaign is because it governs the motion control potential and the monetary cost of TMDs herein treated as TMDIs with very low inertance [13, 49]. Moreover, the parametrization of the inertance is motivated by theoretical studies [13, 28-30] demonstrating that it relaxes requirements for large secondary attached mass for efficient motion control of the PS as well as reduces significantly the kinematics of the secondary mass. Both these considerations are practically important: the former leads, ultimately, to more lightweight and, therefore, economic absorbers; the latter reduces needs for space/clearance to accommodate the absorber, as well as the cost of energy dissipation devices in case fluid dampers are used for the task whose cost increases with the stroke (relative displacement between primary and secondary mass).

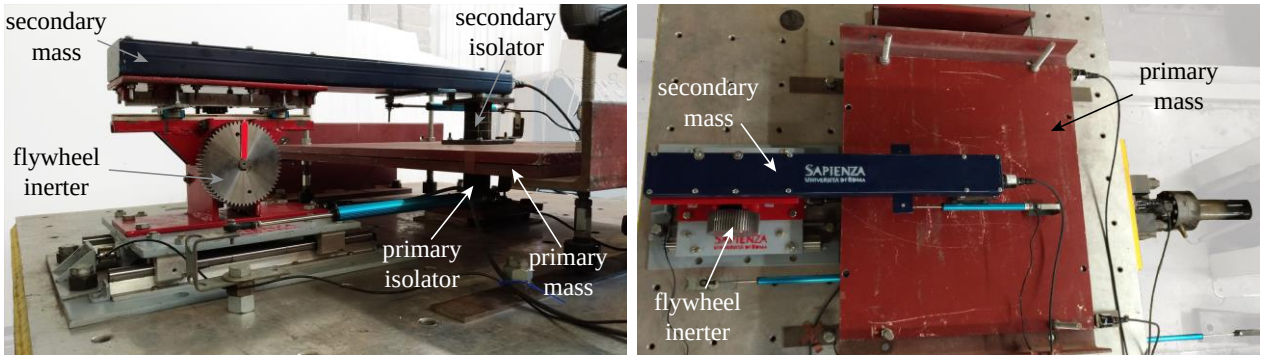

Figure 2. Photos of the experimental setup with the specimen having intermediate mass and large inertance mounted on the shaking table.

In detail, the main mass, $m_I = 125\ kg$, of the physical models consists of two plates with dimensions $0.78\ m \times 0.68\ m \times 0.015\ m$ made of mild steel and jointed through bolts. Further, specimens with three different secondary mass values, m_T, are considered resulting in the mass ratio values, $\mu = m_T/m_I$, reported in Table 1 taken as representatives of TMDI with small, intermediate, and large secondary mass. It is noted in passing that the case of the TID (i.e., a TMDI with zero secondary mass) [12] is not studied herein since a massless/weightless dynamic vibration absorber is physically not feasible: the TID will practically behave as a TMDI with small secondary mass ratio in real-life applications since inerter devices, dampers, and other connecting members will not be massless (see also discussion in [28-29] on the particular case of base-isolated buildings). In the small mass (SM) specimen, a multilayered wood panel (section dimension: $0.10\ m \times 0.025\ m$ and length: $1.25\ m$) with $m_{T,1} = 6\ kg$ is mounted at the top of the secondary isolator. Further, a steel beam with rectangular hollow cross-section (section dimension: $0.10\ m \times 0.05\ m$, thickness: $3\ mm$ and length: $0.80\ m$ shown in the photos of Figure 2) made of mild steel with $m_{T,2} = 10\ kg$ is used in the intermediate mass (IM) specimen. In the large mass (LM) specimen, two steel plates (section dimension: $0.12\ m \times 0.02\ m$, and length: $0.22\ m$) are added to the steel beam reaching a total of $m_{T,3} = 20\ kg$ secondary mass. In this setting, the SM case yields 5% mass ratio which is a common TMD specification for several structures [6]. The LM case is taken as an upper bound of additive

mass one can practically consider in practical TMD implementations. Lastly, the IM serves as one case in between a standard and a heavyweight TMD.

Table 1. Inertial TMDI properties of physical models and inertance/mass ratios $\delta=\beta/\mu$

Inertance ratios	Secondary mass ratios		
	Small mass (SM) ($\mu_1 = 0.048$)	Intermediate mass (IM) ($\mu_2 = 0.080$)	Large mass (LM) ($\mu_3 = 0.160$)
No flywheel (NF) ($\beta_1 = 0.001$)	0.021	0.013	0.006
Intermediate flywheel (IF) ($\beta_2 = 0.383$)	7.800	**4.789**	2.394
Large flywheel (LF) ($\beta_3 = 0.765$)	15.938	9.563	4.781

For both the primary and the secondary isolator, the same circular HDRB is used. It consists of 27 2-mm-thick rubber layers and 26 1-mm thick steel shims. Total rubber thickness is $54\,mm$, while the height of the isolator – excluding the end plates – is $80\,mm$. Total diameter is $58\,mm$, including $53\,mm$ of shim diameter and $5\,mm$ of cover. Oversize end plates permit the isolators to be bolted to the masses. The nominal equivalent stiffness, corresponding to a shear deformation $\gamma = 100\%$, is equal to $k_{nom} = 0.018\,kN/mm$.

Inertance b is provided to all physical models by an inerter device prototype employing a rack-and-pinion mechanism to transform relative translational motion between the secondary mass and the shaking table to rotational motion of a flywheel. An off-the-shelf gearbox with fixed gear ratio 2:1 is used to amplify the flywheel rotational velocity. Herein, physical models with three different inertance values, *b*, are tested corresponding to the inertance ratios $\beta = b/m_I$ reported in Table 1 achieved by changing the flywheel of the inerter prototype. In particular, when no flywheel (NF case) is attached to the inerter, models with very low nominal inertance $b_{1,nom} = 0.1\,kg$ are specified. Further, a flywheel consisting of one spur gear with mass equal to 2.1kg is used in the intermediate flywheel (IF) case achieving nominal inertance $b_{2,nom} = 47.9\,kg$ while a flywheel with

two spur gears shown in the photos of Figure 2, is used in the large flywheel (LF) case achieving nominal inertance $b_{3,nom} = 95.6\ kg$ (i.e., >22 ratio of nominal inertance over flywheel mass).

Shaking table testing for specimens with all the possible, 9, secondary mass and inertance (i.e., TMDI inertial properties) combinations listed in Table 1 are conducted as well as for a physical model with no TMDI attached to the PS serving as the baseline/reference "uncontrolled" structure.

2.3. Test Setup and instrumentation

Testing was carried out on a SDOF shaking table in the Materials Testing Laboratory of the Department of Structural and Geotechnical Engineering of Sapienza University of Rome in Rome, Italy. The $1.50\ m \times 1.50\ m$ shaking table, manufactured by Moog Inc. and managed by Moog Replication Software, has maximum operating frequency $20\ Hz$, maximum acceleration $> \pm 1\ g$, where g is the acceleration of gravity, maximum velocity $> \pm 1\ m/s$, maximum displacement $\pm 0.2\ m$, and can accommodate specimens up to 2 ton of mass.

For the purposes of this work, all tested physical models were instrumented with (see also Figure 3):

- Five piezoeletric ICP® accelerometers, model 393A03 manufactured by PCB Piezotronic. One placed on the shaking table measuring input horizontal ground acceleration, $\ddot{u}_G$; two placed on the main mass measuring total horizontal response acceleration, $\ddot{u}_{I,r}^{(tot)}$ and $\ddot{u}_{I,l}^{(tot)}$, at two different locations as indicated in Figure 3; one placed on the secondary mass measuring total horizontal response acceleration $\ddot{u}_T^{(tot)}$; and one at the inerter support measuring $\ddot{u}_B^{(tot)}$.
- Three displacement sensors, model SLS 190 manufactured by Penny & Giles, measuring relative displacement between (i) the shaking table mass and the lab floor (fixed reference point), u_G, (ii) the primary mass and the shaking table mass, u_I, and (iii) the secondary mass and the primary mass, $u_{TI} = u_T - u_I$.

- A load cell, model U9B manufactured by HBM, to measure the force transmitted by the inerter to the shaking table F_R.

Experimental data were acquired at 500Hz sampling rate through data acquisition system (DAQ) Krypton 3xSTG manufactured by DEWESoft and operated by DEWESoft software. All acquired data series were band-pass filtered by a first order Butterworth filter within the frequency range [0.16Hz 20Hz].

Based on the above measured quantities, the following responses of interest are computed as follows:

- absolute acceleration of the main mass computed by averaging measured main mass accelerations as in

$$\ddot{u}_I^{(tot)} = (\ddot{u}_{I,l}^{(tot)} + \ddot{u}_{I,r}^{(tot)})/2; \quad (1)$$

- relative acceleration of the secondary mass as in

$$\ddot{u}_T = \ddot{u}_T^{(tot)} - \ddot{u}_B^{(tot)}, \quad (2)$$

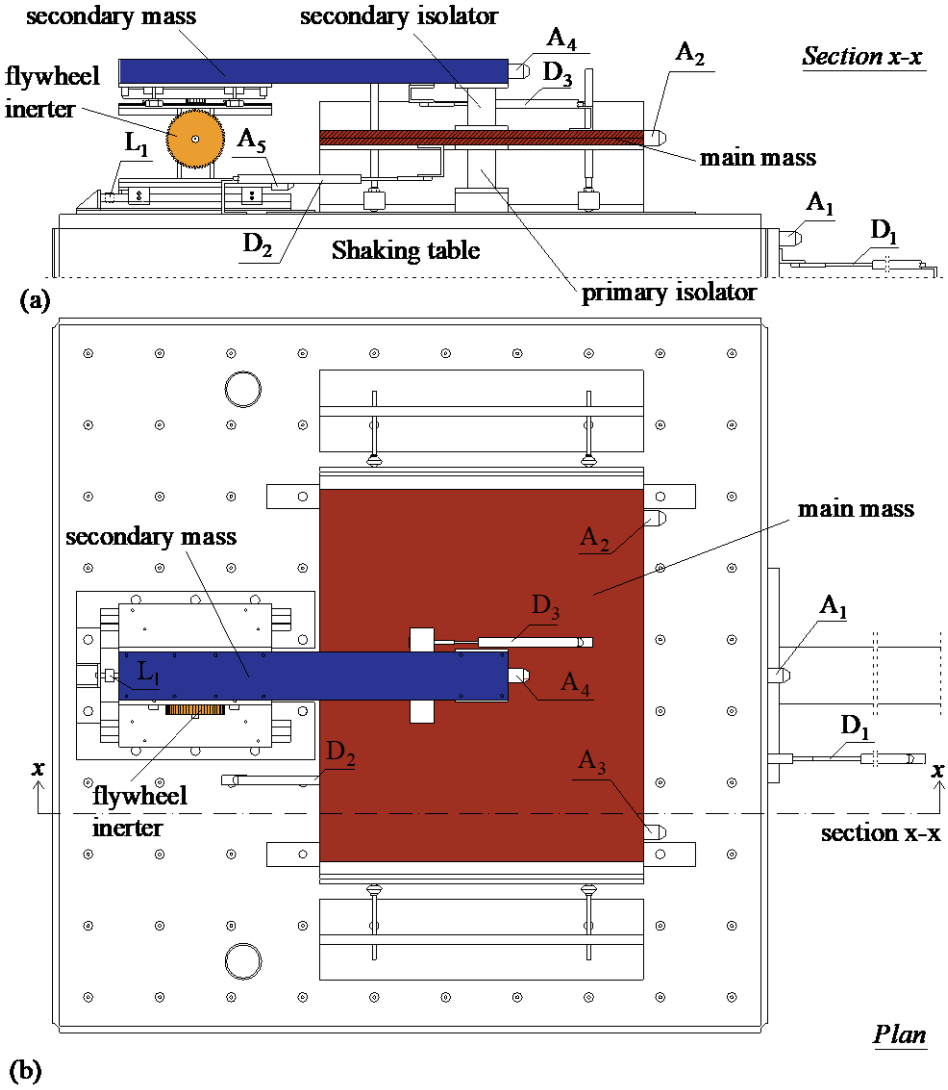

Sensor	A_1	A_2	A_3	A_4	A_5	D_1	D_2	D_3	L_1
Quantity	$\ddot{u}_G$	$\ddot{u}_{I,r}^{(tot)}$	$\ddot{u}_{I,l}^{(tot)}$	$\ddot{u}_T^{(tot)}$	$\ddot{u}_B^{(tot)}$	u_G	u_I	u_{TI}	F_R

Figure 3. Schematic of the experimental setup and instrumentation: (a) section and (b) plan.

where the acceleration $\ddot{u}_B^{(tot)}$ differs insignificantly with respect to $\ddot{u}_G$ as verified during testing;

- relative displacement of the secondary mass respect to the shaking table as in

$$u_T = u_I + u_{TI}; \tag{3}$$

- resisting force generated by the inerter device as in

$$F_B = F_R + m_B \ddot{u}_B^{(tot)}, \tag{4}$$

where m_B is the mass of the inerter device and its support which is equal to 16.7kg for NF models, 18.8kg for IF models, and 20.9kg for LF models;

- resisting force generated at the secondary isolator as in

$$F_T = -F_B - m_T \ddot{u}_T^{(tot)}; \tag{5}$$

- and resisting force generated at the primary isolator as in

$$F_I = F_T - m_I \ddot{u}_I^{(tot)}. \tag{6}$$

All considered physical models have been excited by the shaking table using a sine-sweep signal within the frequency range [1Hz 10Hz] with stepped frequency changes at 0.05Hz near system resonant frequencies and at 0.1Hz away from resonant frequencies. Sine-sweep at both increasing and decreasing frequency in the above range have been applied. At each step, 20 full cycles of excitation were applied to reach steady-state response conditions in order to achieve meaningful frequency domain response signal representations including frequency response functions. Appropriate input/excitation signals in displacement control have been adopted to achieve three different peak acceleration on the shaking table, seen as peak ground acceleration (PGA) by the specimens, namely PGA=0.05g, 0.10g and 0.15g, to span different levels of nonlinear elastic structural behavior. To this effect, note that even under PGA=0.15g, the design shear strain of the isolators is not exceeded.

3. Experimental dynamic response from shaking table testing

This section discusses selective experimental data obtained from shake table testing of the physical models described in the previous section to characterize their response to harmonic base excitation. The presentation starts from investigating response differences as excitation amplitude and frequency varies with discussion focusing mainly on nonlinear behaviour of physical models. To this aim, the uncontrolled PS as well as the PS equipped with TMDI with intermediate mass and inertance are studied. Then, the influence of TMDI inertial properties, inertance and secondary mass,

to the response of physical models is gauged by examining comparatively responses of all 9 physical models with inertial properties listed in Table 1. Throughout this section, experimentally obtained frequency response functions (FRFs), H_p, where p represents the p-th response quantities, normalized with respect to the FRF of base acceleration excitation, $H_{\ddot{u}_G}$, are used to trace response differences to different excitation frequency given as

$$\widehat{H}_p = \frac{H_p}{H_{\ddot{u}_G}} \quad ; \quad p = u_I, \ddot{u}_I^{(tot)}, F_I, u_{TI}, \ddot{u}_T^{(tot)}, F_T, u_T, \ddot{u}_T, F_B \tag{7}$$

3.1. Influence of excitation amplitude and frequency

Physical models tested on the shaking table exhibit nonlinear behaviour deviating from the idealized linear 2-DOF system of Figure 1(a). Herein, deviation from the linear behaviour is appraised by examining the influence of the amplitude and frequency of the sine sweep shaking table excitation to the dynamic response of the physical models. Experimental data pertaining to the main mass response are first discussed followed by examination of response quantities for the TMDI components: secondary mass and isolator (i.e., TMD), as well as inerter device.

Time-histories of main mass displacement, u_I, are plotted in Figure 4 for uncontrolled PS (first row of panels) and for PS equipped with TMDI (second row of panels) measured under sine-sweep excitation of three different peak ground acceleration amplitudes: 0.05g, 0.10g, and 0.15g. The considered TMDI has intermediate mass and inertance (IM-IF), as reported in Table 1, taken as the reference TMDI configuration hereafter. To probe into the nonlinear behaviour of the models' displacement, time-histories obtained by sine-sweep with both increasing and decreasing frequency are superposed in each figure panel. Focusing first on the response of the uncontrolled PS (Figures 4(a-c)), it is seen that peak response (i.e., dynamic amplification) is attained earlier in time as the excitation amplitude increases. This indicates that PS resonates with the sine-sweep excitation at a

lower frequency, hereafter resonance frequency f_0, due to the reduction of the elastomeric isolator effective stiffness with increasing deformation. Indeed, the absolute peak u_I displacement increases from $5\,mm$ for $PGA = 0.05\,g$ excitation amplitude to $38\,mm$ for $PGA = 0.15\,g$ excitation amplitude. Moreover, it is seen that response time-histories for increasing and decreasing sine-sweep excitations do not overlap and the level of non-overlapping becomes more significant with increasing excitation amplitude. Further, peak response is higher and occurs earlier for the sine-sweep with decreasing frequency demonstrating a *softening* nonlinear behavior of the primary elastomeric isolator.

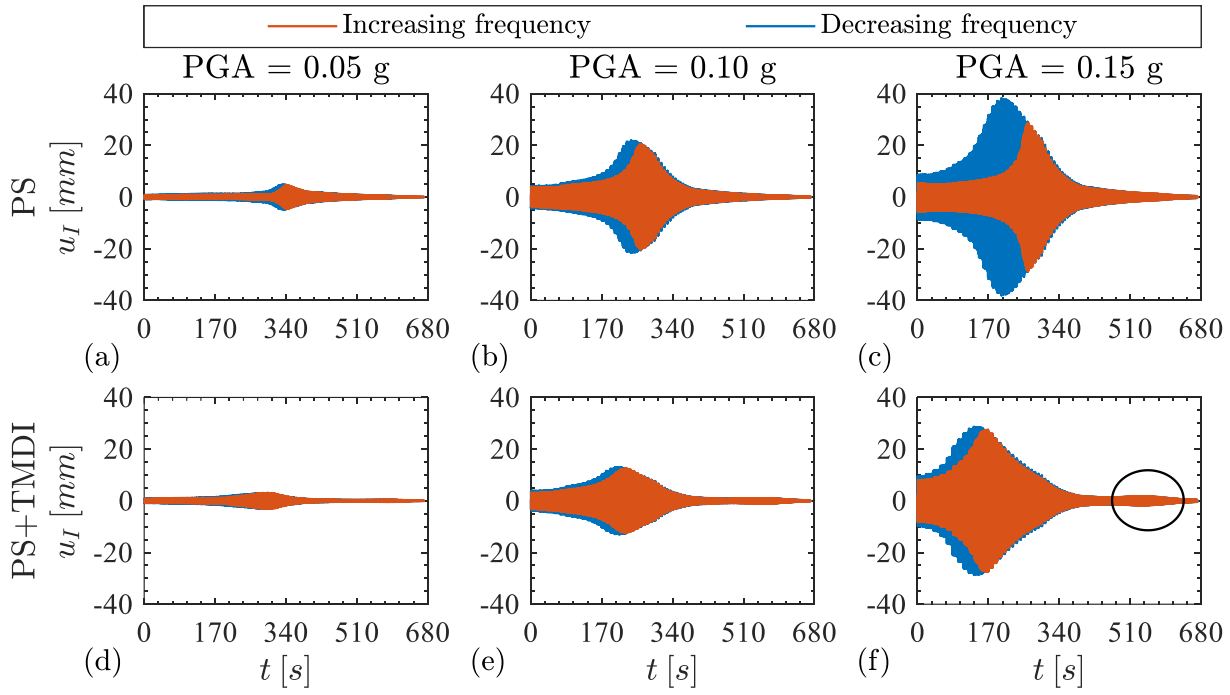

Figure 4. Time histories of PS displacement, u_I, under sine-sweep excitation with increasing and decreasing frequency at 3 different amplitude ($PGA = 0.05, 0.10, 0.15\,g$) for 2 different physical models: (a-c) uncontrolled PS and (d-f) PS+TMDI ($\beta_2 = 0.383$ and $\mu_2 = 0.080$).

Turning the attention to the main mass response of the TMDI-equipped PS model in Figure 4 (d-f), it is seen that the peak PS displacement response, corresponding to first resonance frequency f_1 of the system, is significantly reduced compared to the uncontrolled PS for all excitation amplitudes studied. Specifically, peak PS displacement reductions of 37% is found for $PGA = 0.05\,g$ and 25%

for $PGA = 0.15$. Consequently, nonlinear phenomena are less prominent in the response of TMDI controlled PS compared to the uncontrolled PS for the same excitation amplitude. For example, for $PGA = 0.05\ g$ response time-histories for increasing and decreasing sine-sweep excitations in Figure 4(d) are practically identical (i.e., they overlap), while they deviate significantly less for $PGA = 0.15\ g$ (Figure 4(f)) vis-à-vis the case of uncontrolled PS (Figure 4(c)). Moreover, for TMDI-equipped PS model, a second local peak in the PS response displacement occurs much later in time from the dominant (first) local peak and, therefore, at higher excitation frequency. This second peak goes practically unnoticed for small excitation amplitude and becomes visible for $PGA = 0.15\ g$ indicated in Figure 4(f) by a circle. It is associated with the second (higher) resonance frequency of the TMDI-equipped PS hereafter denoted by f_2.

The above discussed nonlinear behaviour of the physical models and resonant frequencies are further traced in the frequency domain in Figure 5. The latter figure furnishes the magnitude of FRFs, $\widehat{H}_{u_I}$, of PS displacements normalized to FRF of the input acceleration for the same cases examined in Figure 4. These FRFs are obtained by evaluating the maximum stationary value of the response magnitude as a function of excitation frequency. The plotted curves are quite smooth due to the purposely small step used in varying the excitation frequency taken as low as $\Delta f = 0.05Hz$ near resonance frequencies corresponding to local dynamic response amplification. FRFs corresponding to the uncontrolled PS (first row of panels in Figure 5) exhibit a single peak attained at resonance frequency f_0 reported on the figure for both types of sine-sweep excitation (i.e., with increasing and decreasing frequency). It is observed that f_0 values reduce with increasing excitation amplitude and they consistently attain smaller values for sine-sweep excitation with decreasing frequency. Further, peak FRF values are larger for sine-sweep excitation with decreasing frequency vis-à-vis increasing frequency and this discrepancy increases with increasing excitation amplitude. The resulting shape and position of the hysteresis area formed by the differences of the magnitude FRFs for the different

excitation sine-sweeps with fixed amplitude considered are indicative of the *softening* nonlinear elastic behaviour of the primary isolator.

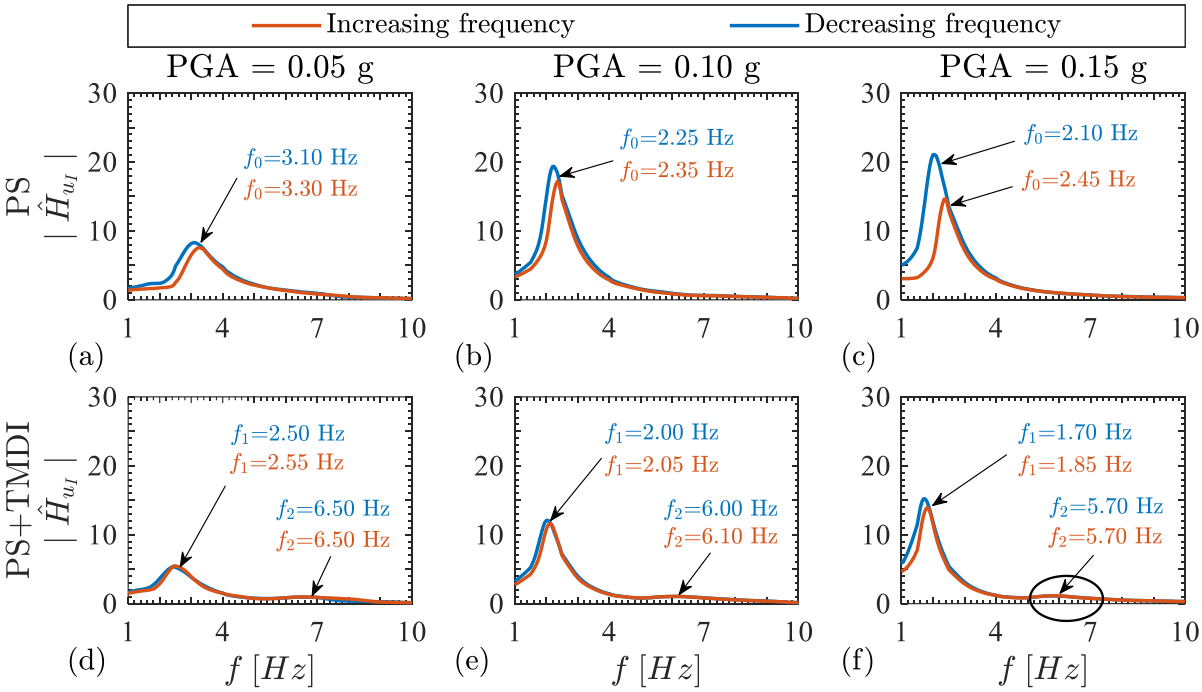

Figure 5. Normalized FRFs of PS displacement under sine-sweep excitation with increasing and decreasing frequency at 3 different amplitude ($PGA = 0.05, 0.10, 0.15\ g$) for 2 different physical models: (a-c) uncontrolled PS and (d-f) PS+TMDI ($\beta_2 = 0.383$ and $\mu_2 = 0.080$).

Examining next main mass displacement FRFs of the TMDI equipped PS (second row of panels in Figure 5), two local peaks are observed corresponding to the two resonant frequencies, f_1 and f_2, with $f_2 > f_1$, as reported in the figure panels with the low-frequency peak being significantly more prominent. It is seen that both f_1 and f_2 decrease with increasing excitation amplitude indicating, again, a *softening* nonlinear elastic behaviour. This shift towards lower frequencies is more significant for the low resonance frequency, f_1, as it is related to higher levels of dynamic amplification (i.e., higher FRF ordinate). For instance, f_1 reduces by 32% as excitation amplitude increases from $PGA = 0.05\ g$ to $PGA = 0.15\ g$, while f_2 reduces by only 12% for the same change in excitation amplitude. Moreover, for fixed *PGA*, resonance frequency f_0 corresponding to the uncontrolled PS lie always in between the resonance frequencies of the TMDI equipped PS, that is, $f_1 < f_0 < f_2$. The latter observation confirms complex modal analysis results reported in De Angelis et al. [30] applied to the

idealized linear system of Figure 1(a). Further, FRFs obtained by different sine-sweep excitation phases (i.e., increasing and decreasing frequency in time) overlap practically everywhere except from frequencies lower than the f_1 obtained by the sweep-sine excitation with increasing frequency, while the "hysteresis area" formed by the difference of the FRFs is much smaller for the same excitation compared to the uncontrolled PS. Overall, FRFs reported in Figure 5 demonstrate the effectiveness of the TMDI to suppress peak PS displacement and, consequently, TMDI equipped PS exhibits weaker nonlinear response phenomena than uncontrolled PS.

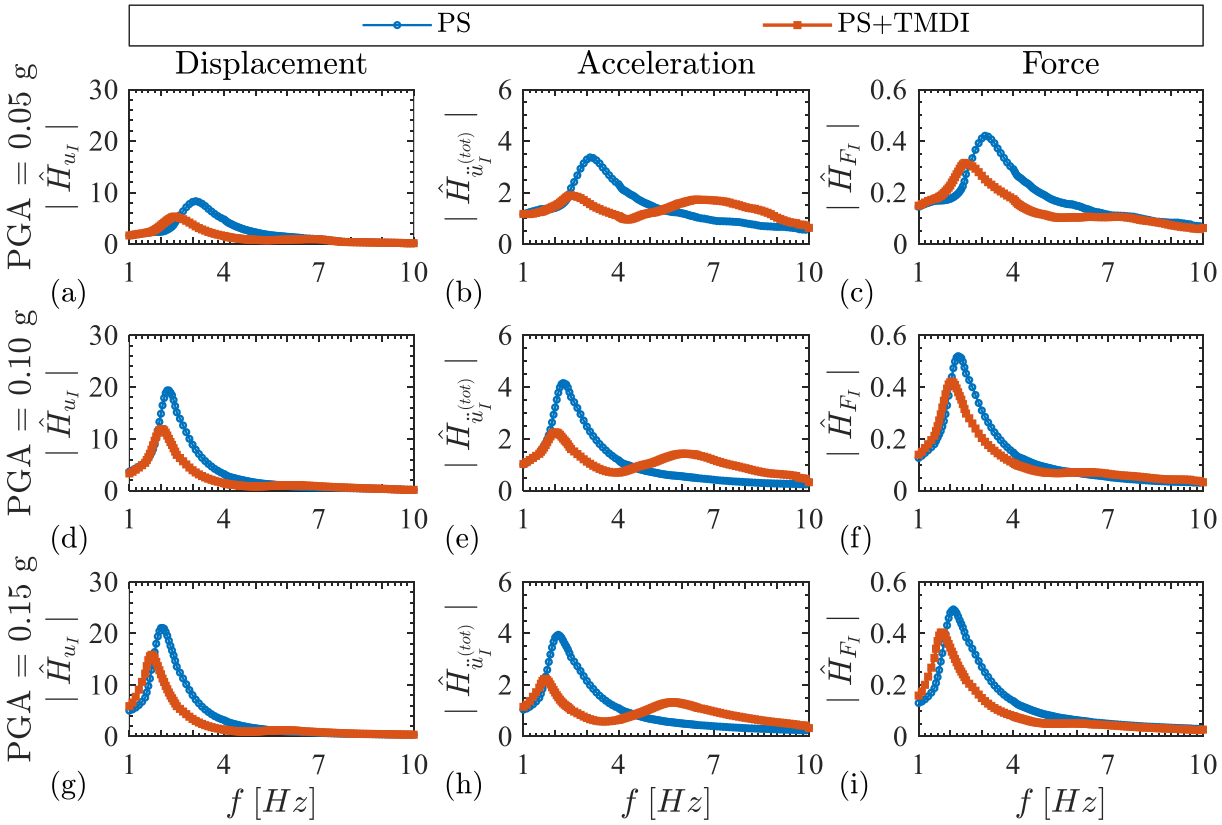

Figure 6. Normalized FRFs of (a-c) PS displacement, (d-f) PS acceleration, and (g-f) primary isolator shear force, under sine-sweep excitation with decreasing frequency at 3 different amplitude ($PGA = 0.05, 0.10, 0.15\ g$) for uncontrolled PS and for PS+TMDI ($\beta_2 = 0.383$ and $\mu_2 = 0.080$).

To further highlight differences to the response amplitude of the uncontrolled PS and PS controlled with the reference (IM-IF) TMDI, Figure 6 plots FRFs of the two physical models vis-a-vis in terms of PS displacement, PS acceleration, and primary isolator shear force for three different excitation amplitudes and for sine-sweep with decreasing frequency. It is seen that the considered

TMDI reduces both peak PS displacement and PS base shear for all excitation frequencies except from the low-frequency range $f < f_0$ where small amplification is observed. Nevertheless, this is not the case for PS acceleration which are significantly reduced near PS resonance frequency, f_0, but amplified at higher frequency excitations near f_2. This is because response acceleration is significantly influenced by high frequency system dynamics introduced by the inclusion of the TMDI. This may be better appreciated by noting that the inclusion of the TMDI to the idealized system of Figure 1(a) introduces a second DOF and, consequently, one higher resonant frequency associated with a mode shape in which typically the main and the secondary mass are displaced in opposite directions. This behaviour is verified experimentally as shown in Figure 7 plotting displacements of the main mass, m_I, and secondary mass, m_T, at time instant $\bar{t}$ when uncontrolled PS displacement is maximised, $u_{I0,max}$, normalized by this displacement for different excitation amplitude and for excitation frequency coinciding with the resonance frequencies f_1, f_0 and f_2. It is seen that for the higher resonance frequency f_2 the main and secondary masses move out of phase and in alignment with a theoretically expected second mode of vibration.

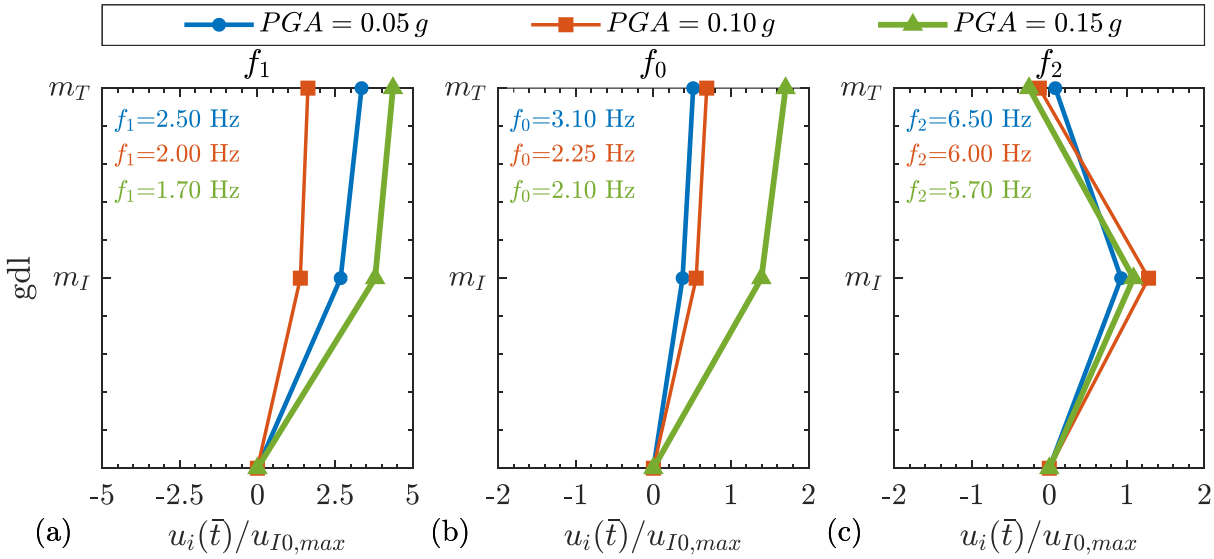

Figure 7. Concurrent displacements u_i, with $i = I, T$, of main and secondary mass at the time of main mass peak displacement normalized by $u_{I0,max}$ for the TMDI controlled PS ($\beta_2 = 0.383$ and $\mu_2 = 0.080$) under different excitation amplitude at excitation frequencies: (a) f_1, (b) f_0, and (c) f_2.

Shedding further light to the behaviour of the TMDI, Figure 8 plots FRFs related to the response of the secondary mass as well as to the inerter under different excitation amplitude. It is observed that the peak stroke in Figure 8(a), relative displacement between primary and secondary mass, is relatively insensitive to the excitation amplitude and frequency compared to peak primary and secondary mass displacements in Figure 5(d-f) and Figure 8(d), respectively, as well as significantly lower in amplitude. Similar to PS acceleration FRF, secondary mass acceleration FRF in Figure 8(b) observes two local peaks at frequencies f_1 and f_2, which become more prominent as excitation amplitude increases. The FRF of the control force transmitted from the TMDI to the PS in Figure 8(c) is largely broadband for low excitation amplitude being almost constant within the frequency range $f_1 < f < f_2$, while, as the excitation amplitude increases, higher control forces at resonance frequencies f_1 and f_2 develop and become more prominent.

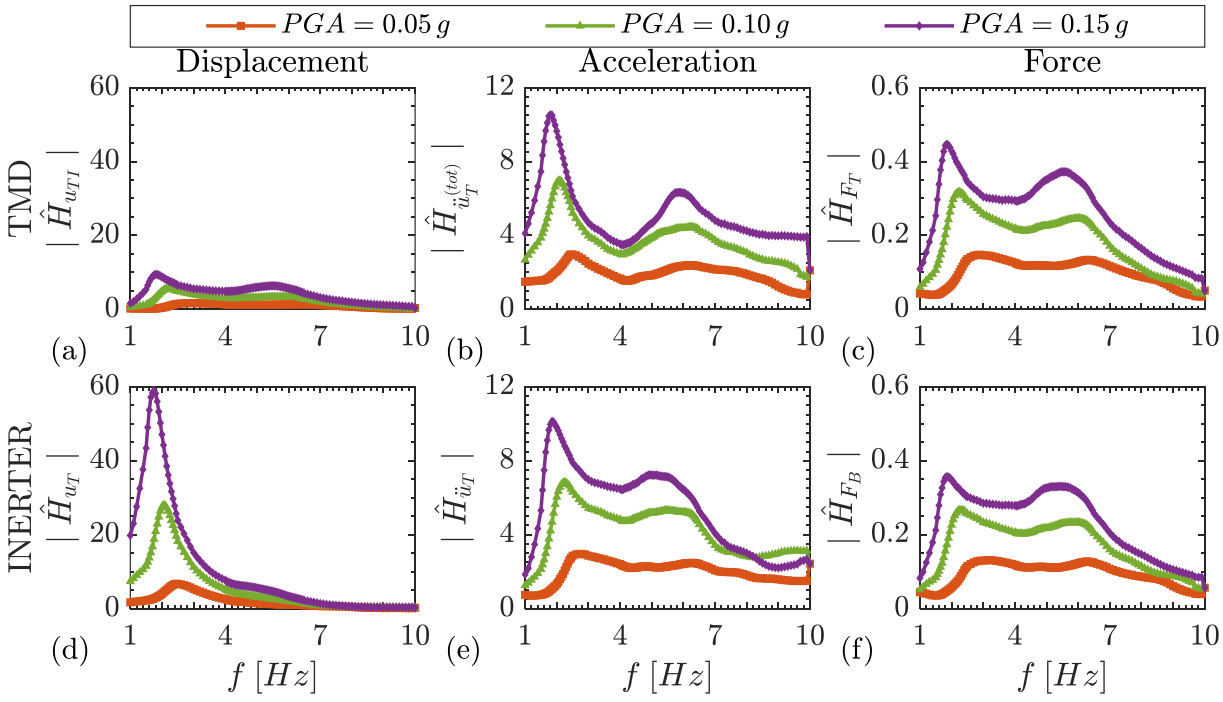

Figure 8. Normalized FRFs of (a) TMDI stroke, (b) secondary mass acceleration, (c) secondary isolator shearing force, (d) secondary mass displacement, (e) inerter relative acceleration , and (f) inerter force under sine-sweep excitation with decreasing frequency at 3 different amplitudes for TMDI controlled PS ($\beta_2 = 0.383$ and $\mu_2 = 0.080$).

Secondary mass displacement FRFs in Figure 8(d) follow similar trends with PS displacement FRFs in Figure 5, while FRFs of inerter relative acceleration and force in Figure 8(e) and Figure 8(f), respectively, follow similar trends with the control force transmitted from the secondary isolator to the main mass in Figure 8(c). The latter observation verifies experimentally the key role of the grounded inerter to the effectiveness of the TMDI for vibration suppression as has been reported in previous analytical and numerical studies investigating the idealized system of Figure 1(a) [13, 17, 49].

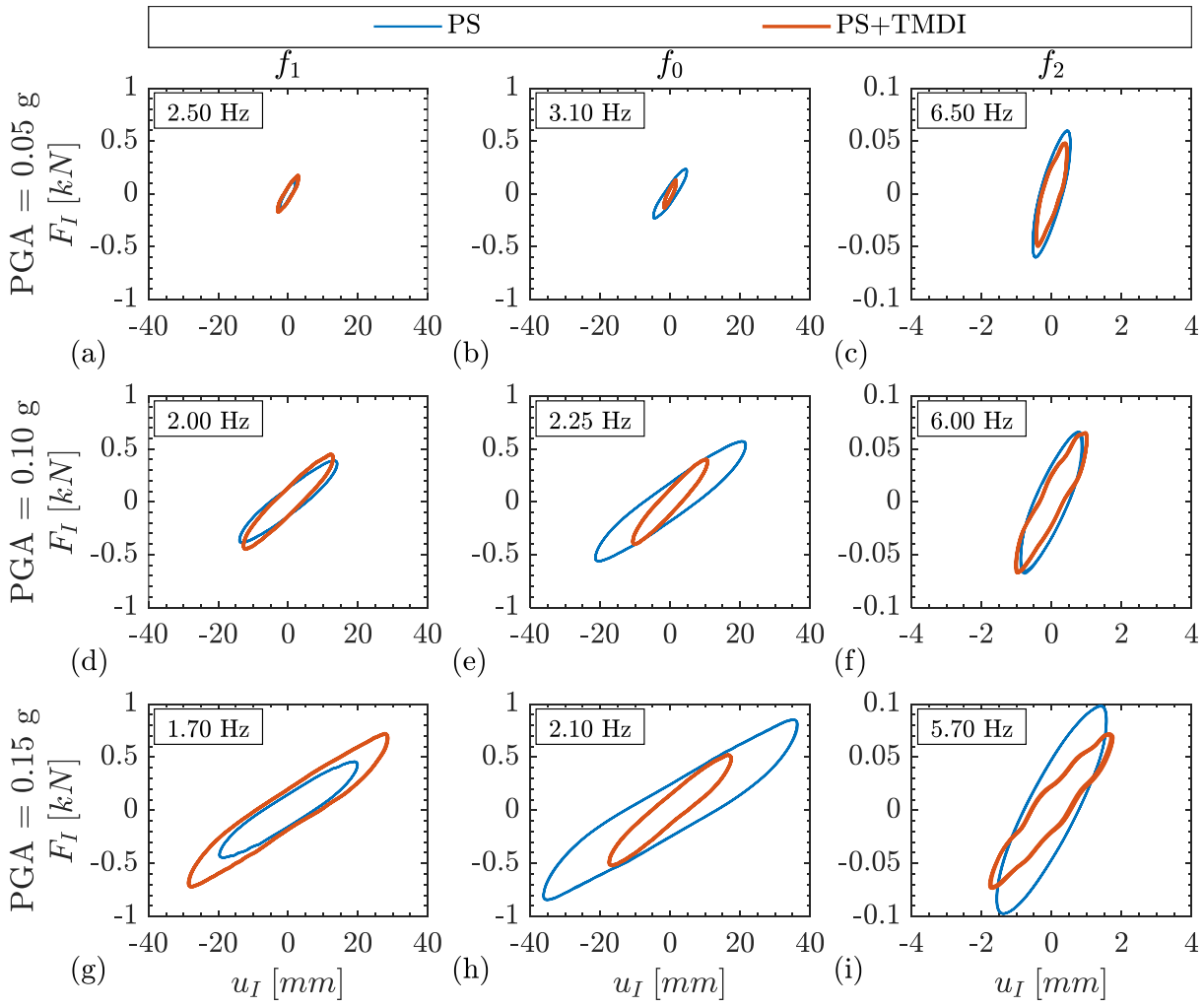

Figure 9. Force-deformation curves, $F_I - u_I$, of uncontrolled PS and for TMDI controlled PS ($\beta_2 = 0.383$ and $\mu_2 = 0.080$) at resonance frequencies f_I, f_0 and f_2 for (a-c) $PGA = 0.05g$, (d-f) $PGA = 0.10g$ and (g-i) $PGA = 0.15g$.

The deviation of the physical specimens from the linear behaviour with increasing excitation amplitude at different critical excitation frequencies is further captured by the force-deformation curves of the primary isolator, $F_I - u_I$, shown in Figure 9. The presented data are for the uncontrolled PS and for the reference TMDI-equipped PS for the three previously considered excitation amplitudes and for excitation frequency equal to the resonance frequencies f_1, f_0, and f_2. The area of the hysteretic loops developing at fixed excitation frequency increases with increasing response (and excitation) amplitude for both systems. Significantly more energy is dissipated by the primary isolator of the uncontrolled specimen excited at the PS resonant frequency, f_0, compared to the TMDI controlled system, while more energy is dissipated by the primary isolator of the TMDI controlled specimen at excitation frequency f_1. The above trends are further verified for the secondary isolator as evidenced by force-deformation curves $F_T - u_{TI}$, in Figure 10(a) for the PS with reference TMDI at frequency excitations pinned to the resonance frequencies f_1, f_0 and f_2 and for $PGA = 0.10\ g$ excitation. It is seen that more energy is dissipated as the response amplitude increases due to changes in the excitation frequency. Moreover, force-deformation curves for the inerter device, $F_B - u_T$, plotted in Figure 10(b) for the same structures and excitations as before demonstrate that the inerter does behave as a "negative stiffness" device (see also [50]) as the obtained curves do trace a backbone with a negative average slope. The latter slope is frequency-dependent and increases with frequency while negligible hysteresis is observed for the high-frequency excitation f_2 which is also associated with lower inerter displacement amplitude.

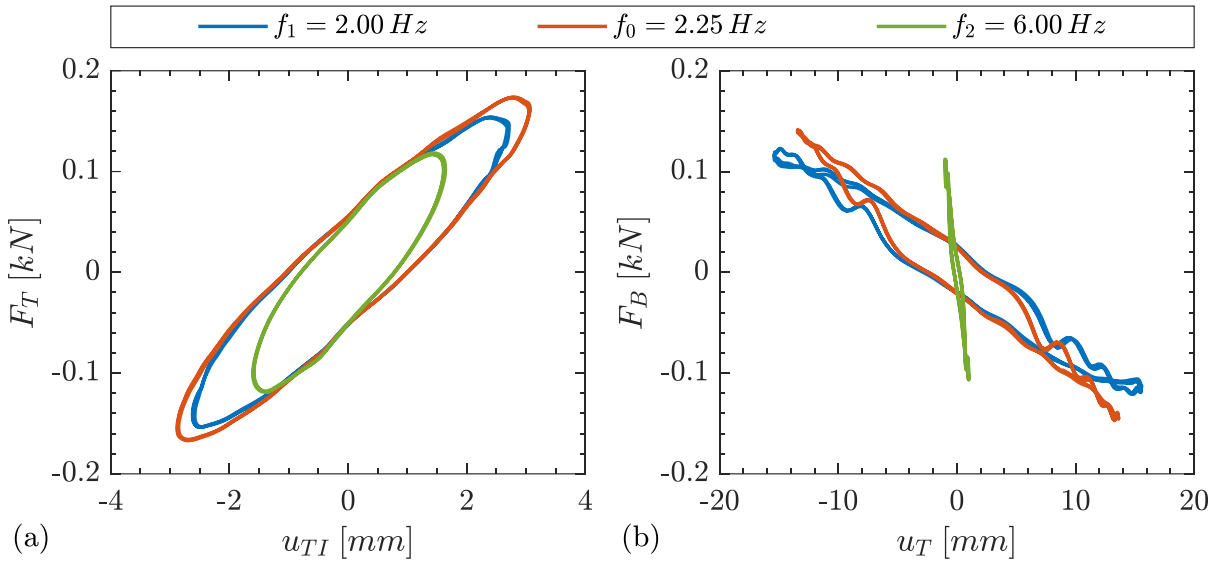

Figure 10. Force-deformation curves (a) $F_T - u_{TI}$ and (b) $F_B - u_T$ of TMDI controlled PS ($\beta_2 = 0.383$ and $\mu_2 = 0.080$) under f_I, f_0 and f_2 excitation frequencies and $PGA = 0.10g$ excitation amplitude.

3.2. Influence of inertance

Having established the influence of the excitation properties to the harmonic response of the physical models, attention is now focused on investigating the influence of the inertance of the TMDI property associated with the number of flywheels mounted on the inerter prototype as described in section 2.2 (see also Table 1). In this section, excitation amplitude is fixed at PGA = 0.10g and secondary mass ratio at $\mu = 0.080$, while response data for TMDI-equipped PS with three different inertance values reported in Table 1 as well as for the uncontrolled PS are presented vis-à-vis.

Figure 11 plots 9 FRFs of displacement, acceleration, and force quantities (column-wise panel arrangement in the figure) relevant to the three different components of the physical model, namely PS (i.e. primary isolator and mass), TMD (i.e. secondary isolator and mass), and inerter device (row-wise panel arrangement in the figure). It is seen that both the two natural resonance frequencies f_1 and f_2 (i.e., location of local FRF peaks) of the TMDI-equipped models decrease with increasing

inertance, with the second resonance frequency mostly evident in the acceleration response of the primary and secondary mass. Further, FRF displacement and acceleration amplitudes at f_1 frequency reduce with increasing inertance and the same is seen for the shearing force developing at the primary isolator. These trends confirm analytically derived results pertaining to the 2-DOF idealized system in Figure 1(a) demonstrating that TMDI becomes more effective in containing peak primary structure response as the inerter coefficient increases for same secondary mass (e.g., [13, 17]). Note, however, that PS absolute acceleration amplitude at f_2 excitation frequency increases with increasing inertance as evidenced in Figure 11(b) which demonstrates that increase of inertance is not necessarily beneficial across all excitation frequencies and response quantities. Lastly, the FRFs of the TMDI control force exerted to the main mass as well as of the inerter force are rather flat/broadband and increase significantly going from negligible inertance (NF) to intermediate inertance (IF), but not quite as much going from IF to large inertance (LF). There is, thus, a saturation of the developing forces within the TMDI with increase of inertance.

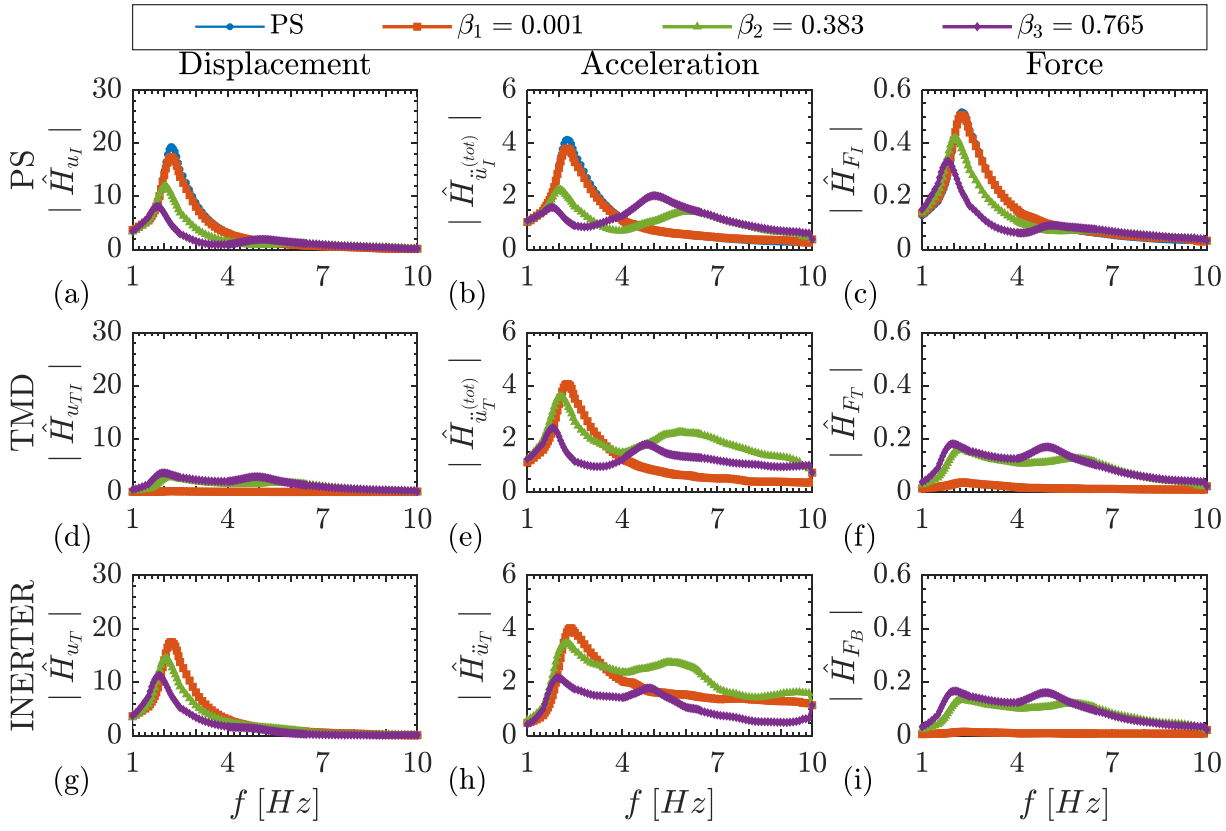

Figure 11. Normalized FRFs of (a) primary mass displacement, (b) primary mass acceleration, (c) primary isolator shearing force, (d) TMDI stroke, (e) secondary mass acceleration, (f) secondary isolator shearing force, (g) secondary mass displacement, (h) inerter relative acceleration, and (i) inerter of TMDI controlled PS with mass ratio μ=0.080 and various inertance ratios under sine-sweep excitation with *PGA*=0.10g.

The influence of the inertance to force-deformation curves of the primary isolator, secondary isolator, and inerter device as well as to the inerter force-acceleration curve is investigated in Figure 12 which furnishes all relevant curves for f_0 excitation frequency. It is seen that energy dissipation at the primary isolator is significantly reduced with increasing inertance, while the opposite happens at the secondary isolator. This observation confirms analytical results for the idealized 2-DOF linear system in Figure 1(a) reported in De Angelis et al. [30] demonstrating that the inertance value leverages energy dissipated by the TMDI and a primary isolated structure. Note in passing that as inertance increases, the effective stiffness of the primary and the secondary isolator increases and decreases, respectively and the opposite happens to their peak deformation. Data plotted in Figure 12(c,d) confirm experimentally that the addition of flywheels to the inerter device increases its effective inertance value: both the negative and the positive average slopes of the closed-loop curves in Figure 12(c) and 12(d), respectively, increase with increasing inertance. There is significant deviation of the experimentally derived force-relative acceleration relationship of the inerter prototype device considered herein compared to an ideal inerter element in Figure 12(d). Nevertheless, inerter force-deformation curves in Figure 12(c) are much smoother than those in in Figure 12(d), and even smoother are the force-deformation curves of the two isolators. The latter observation leads to the practical conclusion that deviation of the inerter device behavior from the ideal linear inerter element behaviour does not influence significantly PS response and, therefore, may not be an important consideration in TMDI design analysis and assessment. Further evidence to reinforce the above conclusion is provided Section 4.2 with the aid of data derived from pertinent numerical nonlinear modelling.

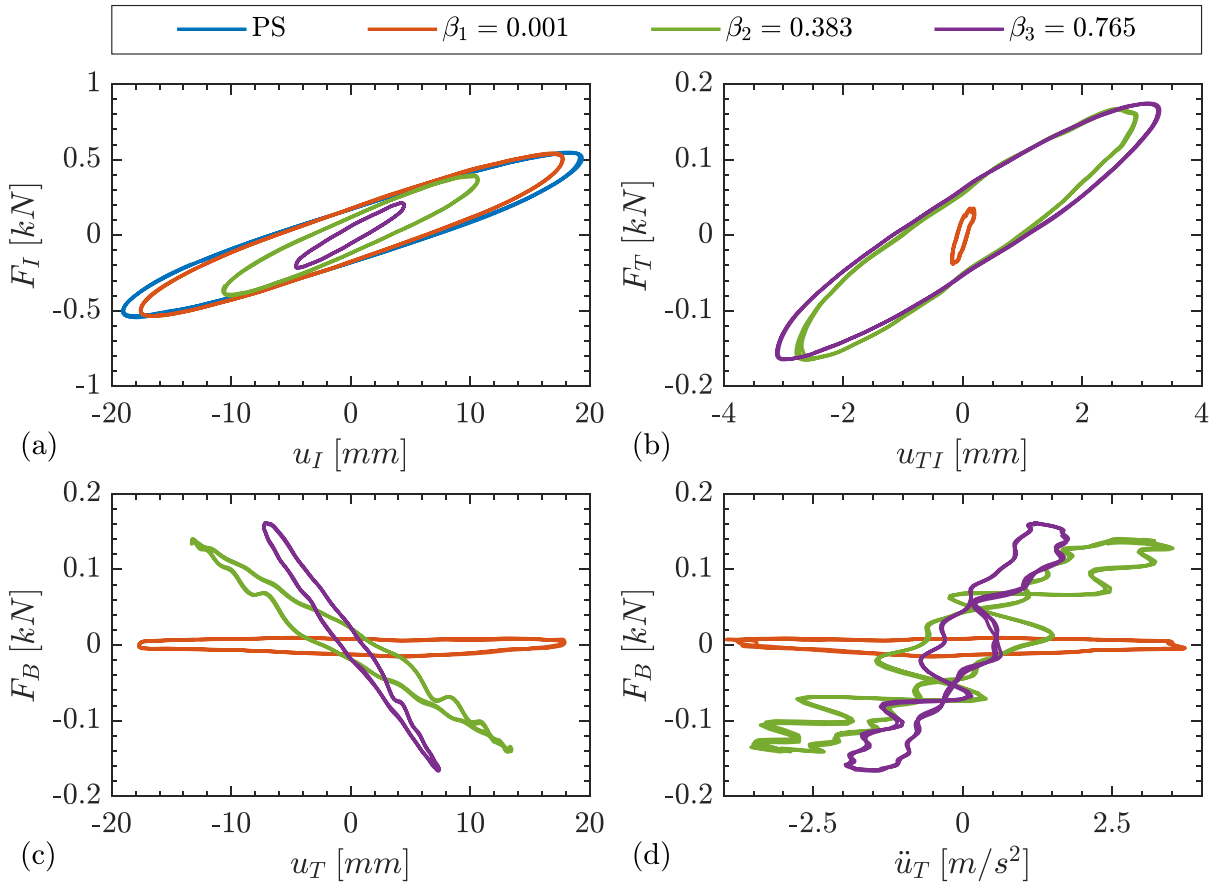

Figure 12. Force-deformation curves (a) $F_I - u_I$, (b) $F_T - u_{TI}$, (c) $F_B - u_T$, and (d) $F_B - \ddot{u}_T$ for of TMDI controlled PS with mass ratio μ=0.080 and various inertance ratios under harmonic excitation with *PGA*=0.10g and at frequency $f_0 = 2.25\ Hz$.

3.3. Influence of secondary mass

In analogy to the previous sub-section, herein the influence of the TMDI/secondary mass property is studied by furnishing response data for the same excitation as before for TMDI-equipped PS with three different secondary mass values reported in Table 1 and fixed inertance to the IF case. Figure 13 plots the same FRFs as in Figure 11 for physical models with 3 different secondary mass and fixed inertance. Evidently, increasing secondary mass ratio affects detrimentally PS displacement and secondary mass displacement and acceleration. This observation confirms previous theoretical studies [13, 17, 30] demonstrating that TMDI becomes more effective as secondary mass reduces as long as sufficient inertance is provided.

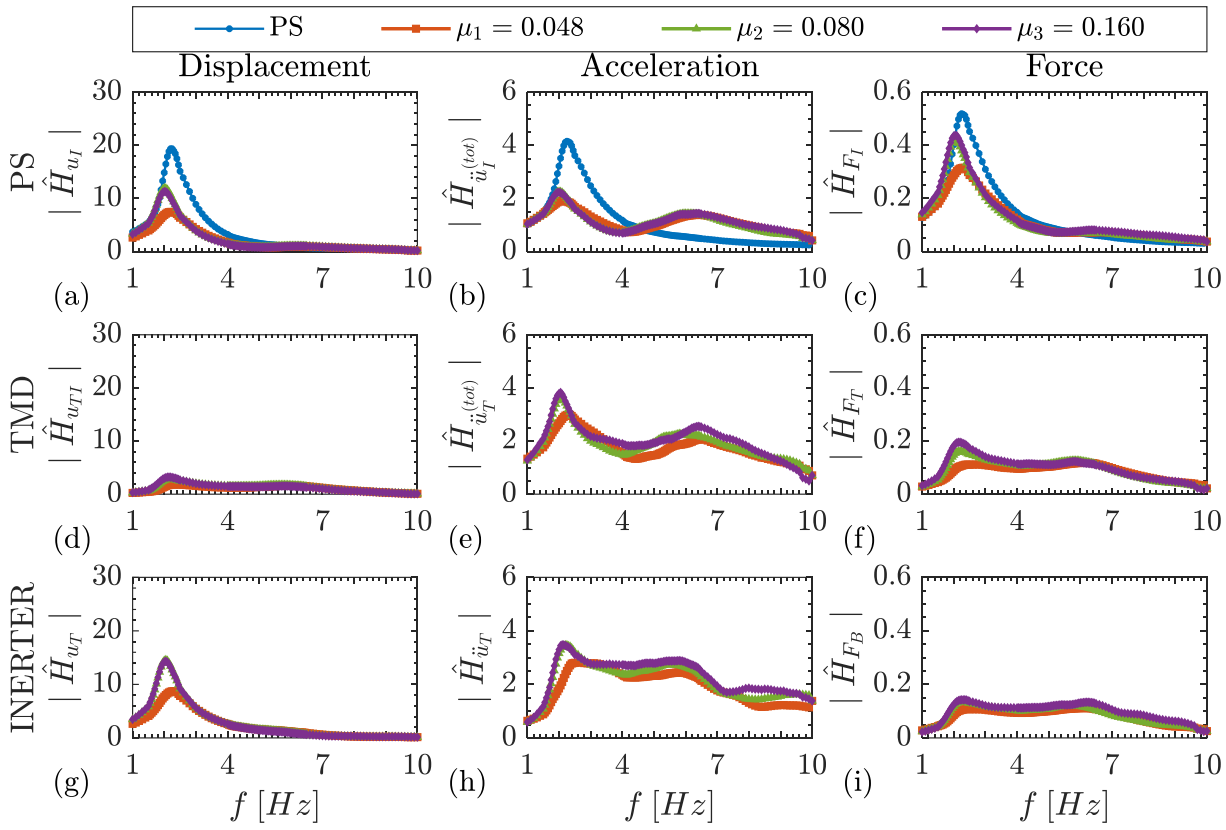

Figure 13. Normalized FRFs of (a) primary mass displacement, (b) primary mass acceleration, (c) primary isolator shearing force, (d) TMDI stroke, (e) secondary mass acceleration, (f) secondary isolator shearing force, (g) secondary mass displacement, (h) inerter relative acceleration, and (i) inerter of TMDI controlled PS with inertance ratio $\beta = 0.383$ and various mass ratios under sine-sweep excitation with *PGA*=0.10g.

Similar conclusions are drawn on the influence of the secondary mass by examining response data plotted in Figure 14, being the same in nature as those of Figure 12 but for varying the secondary mass ratio and for fixed inertance ratio equal to β=0.383. Force-deformation curves of the primary isolator in Figure 14(a) are close to each other for the three TMDI controlled models with those for μ=0.080 and μ=0.160 being almost identical. More difference among force-deformation curves is noted for the case of the secondary isolator which dissipates significantly more energy by increasing the attached mass from μ= 0.048 to μ=0.080 in Figure 14(b). Inerter force-relative acceleration plots in Figure 14(d) are overly irregular, though they all observe a similar average slope (inertance) close to 47.9kg which is the nominal inertance for the case considered (β=0.383), while the inerter force-

deformation curves in Figure 14(c) are less irregular. Focusing on the latter set of curves, it is seen that inerter force-deformation for the the specimen with the smallest secondary mass (μ= 0.048) deviates significantly from the other two specimens and from the ideal linear inerter element behavior. This is because the inerter device is non-linear and, therefore, its behavior depends on the device deformation amplitude and speed which, in turn, depends on the specimens properties for fixed excitation, including the secondary mass. Evidently, in the case of smallest inerter stroke which corresponds to the specimen with the lowest secondary mass (μ= 0.048) the effects of the nonlinearities, such as those due to play of the gears and inernal friction discussed in [46] and in the next section, are more evident compared to cases with larger inerter stroke corresponding to specimens with larger secondary mass. This is a common trend in flywheel rack-and-pinion inerters [34]. Still, primary isolator force-deformation curves are smooth confirming that inerter device nonlinear behaviour may have little effect to PS response dynamics. Collectively, it is found that variations to the inertance influences response dynamics much more significantly than similar percentage variations to the secondary mass.

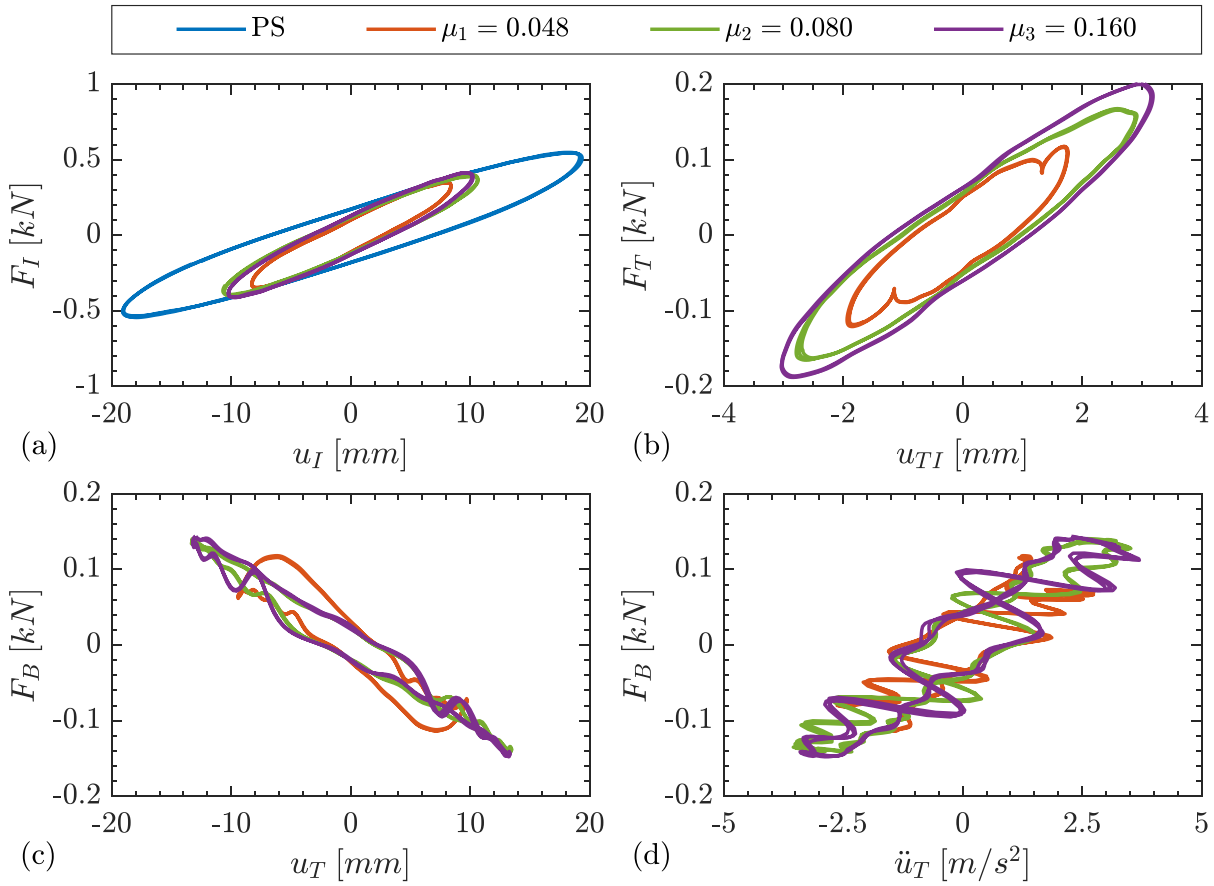

Figure 14. Force-deformation curves (a) $F_I - u_I$, (b) $F_T - u_{TI}$, (c) $F_B - u_T$, and (d) $F_B - \ddot{u}_T$ for of TMDI controlled PS with inertance ratio β=0.383 and various mass ratios under harmonic excitation with *PGA*=0.10g and at frequency $f_0 = 2.25\ Hz$.

4. Nonlinear numerical model

The dynamic response of the physical system in Figure 2 is characterized numerically in this section by first defining a parametric nonlinear 2-DOF numerical model and then calibrating model parameters to shaking table experimental data through the solution of an optimization problem. A variant nonlinear numerical model is further considered which assumes ideal inerter behaviour and its response is compared to the experimental data to gauge the effect of deviating from the ideal inerter element behaviour to the motion control potential of TMDI for nonlinear structures.

4.1. Parametric definition of the numerical model and equations of motion

A nonlinear 2-DOF numerical model is used to approximate the response of the physical model in Figure 2 under shaking table excitations examined in previous sections. Naturally, the DOFs correspond to the lateral translations of the main mass, m_I, and secondary mass, m_T, expressed by the relative to the ground displacements u_I and u_T, respectively as seen in Figure 15.

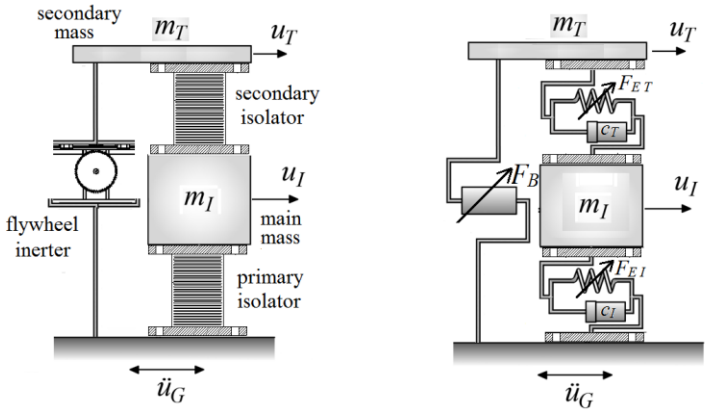

Figure 15. Nonlinear 2-DOF numerical model characterizing the physical system of Figure 2. The arrow above an element indicates nonlinear element behaviour.

The rheological model adopted to capture the nonlinear behaviour of the two HDRB isolators for the developed shear strains induced during the considered experiments consists of a linear dashpot in parallel with a nonlinear elastic spring as graphically shown in Figure 15. The dashpot accounts for the expected energy dissipation by the HDRBs in a simplified but adequate fashion for the testing campaign at hand given the range of shear strains experienced by the isolators [50]. In modelling the nonlinear HDRB stiffness, piecewise nonlinear force-displacement models (e.g., bilinear, trilinear, etc.) [50] or continuous smooth nonlinear functions [51] can be used. Herein, the second approach is taken and nonlinear elastic spring following a third-order polynomial function with the displacement is assumed. Overall, the force-deformation relationships used in the modelling of the two HDRBs are written as

$$\begin{aligned} F_{EI} &= k_{1I}u_I + k_{2I}u_I^2 sign(u_I) + k_{3I}u_I^3, \;\; F_{DI} = c_I\dot{u}_I \\ F_{ET} &= k_{1T}u_{TI} + k_{2T}u_{TI}^2 sign(u_{TI}) + k_{3T}u_{TI}^3, \;\; F_{DT} = c_T(\dot{u}_T - \dot{u}_I) \end{aligned} \tag{8}$$

where F_{EI} and F_{DI} are the resisting forces of the nonlinear spring and the dashpot, respectively, used in the modelling of the main isolator and $F_{E\,T}$ and F_{DT} are the corresponding forces relevant to the secondary isolator. In the last expressions, k_{jI} and k_{jT} (j=1,2,3) are coefficients characterising the behaviour of the primary and secondary nonlinear spring, respectively, while c_I and c_T are the damping coefficients for the primary and secondary isolators, respectively. Further, a dot over a symbol denotes differentiation with respect to time and $sign(\cdot)$ symbolizes the signum function, that is, $sign(x) = 1$ for $x > 0$ and $sign(x) = -1$ for $x < 0$.

Moreover, the inerter device used in the physical models is represented numerically by the mechanical model shown in Figure 16. In the latter model, r_P is the radius of the pinion transforming the translational into rotational motion, while J_B is the flywheel moment of inertia. The model accounts for friction effect of the rack-and-pinion mechanism of the device through the coulomb friction element with coefficient f_y as well as parasitic damping through the dashpot with coefficient c_B. It further accounts for the so-called "play effect" of the inerter (see e.g., [53]) through a double-sided backlash gap with ε_1 and ε_2 clearances. This gap element is connected in series with a visco-elastic element, following the work Papageorgiou et al. [34], with stiffness k_s and damping c_s.

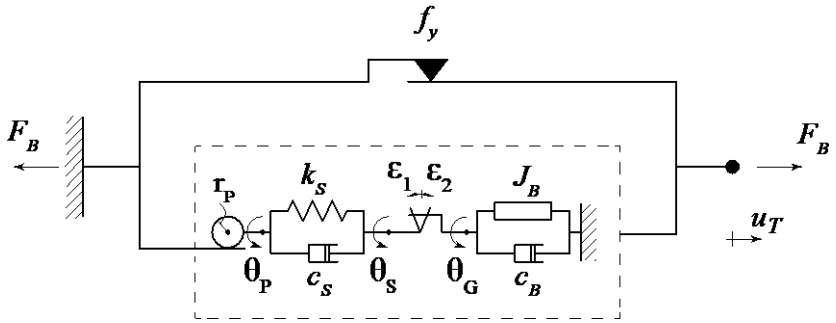

Figure 16. Adopted nonlinear mechanical model characterizing the rack-and-pinion flywheel-based inerter included in the physical models.

Ultimately, the three different rotational DOFs, θ_P, θ_S, and θ_G, shown in Figure 16 are used to define the torques developed at the internal elements in the adopted mechanical model given as

$$T_P = k_S(\theta_S - \theta_P) + c_S\left(\dot{\theta}_S - \dot{\theta}_P\right) \text{ and } T_G = J_B\ddot{\theta}_G + c_B\dot{\theta}_G, \tag{9}$$

where $\theta_P = u_T/r_P$. The nonlinear force-deformation relationship characterizing the behaviour of the prototype inerter device is written as

$$F_B = f_y sign(\dot{u}_T) + T_P/r_P \tag{10}$$

where

$$\begin{cases} T_P = T_G \leq 0 & \text{for} \quad \theta_G - \theta_S = -\varepsilon_1 \\ T_P = T_G = 0 & \text{for} \quad -\varepsilon_1 < \theta_G - \theta_S < \varepsilon_2 \\ T_P = T_G \geq 0 & \text{for} \quad \theta_G - \theta_S = \varepsilon_2 \end{cases} \tag{11}$$

Having defined analytically force-deformation relationships for the two isolators and the inerter device in Eqs (8) and (10), the equations of motion of the nonlinear 2-DOF numerical model in Figure 15 are written as

$$\begin{aligned} m_I\ddot{u}_I + F_I &= -m_I\ddot{u}_G + F_T \\ m_T\ddot{u}_T &= -m_T\ddot{u}_G - F_B - F_T \end{aligned} \tag{12}$$

where $F_I = F_{EI} + F_{DI}$ and $F_T = F_{ET} + F_{DT}$.

4.2. Identification of HDRB parameters and comparison of numerical with experimental data

The nonlinear 2-DOF parametrically defined model of Figure 15 is herein calibrated against selective experimental shaking table response data to capture the response of the reference physical system with intermediate properties specified in Table 1: β = 0.383 and μ = 0.080. The inertial

properties of the considered physical system as well as the 8 parameters involved in the nonlinear force-deformation relationship of the inerter prototype are taken as known and fixed as: $m_I = 125\ kg, m_T = 10\ kg, f_y = 7.3\ N, r_P = 0.018\ m, J_B = 1.55 \times 10^{-2}\ kgm^2, k_S = 187.16\ Nm/rad,$ $c_S = 0.85\ Nms/rad$, $\varepsilon_1 = 0.0084\ rad$, $\varepsilon_2 = 0.0056\ rad$ and $c_B = 0.03\ Nms/rad$. The parameters of nonlinear inerter model have been determined based on optimal fitting to experimental data obtained from inerter component-only shaking table testing as detailed in Pietrosanti [52].

Therefore, herein, the unknown model parameters (i.e., to be calibrated against the experimental data) are the 8, in total, coefficients involved in the definition of the rheological models for the two isolators (i.e., one damping coefficient and three nonlinear spring coefficients per isolator). The known and the unknown model parameters are collected in vectors $\boldsymbol{x}_1$ and $\boldsymbol{x}_2$, respectively, specified as:

$$\begin{aligned} \boldsymbol{x}_1 &= [m_I, m_T, f_y, r_P, J_B, k_S, c_S, \varepsilon_1, \varepsilon_2, c_B]^T \\ \boldsymbol{x}_2 &= [k_{1I}, k_{2I}, k_{3I}, c_I, k_{1T}, k_{2T}, k_{3T}, c_T]^T \end{aligned} \tag{13}$$

The parameters in $\boldsymbol{x}_2$ vector are determined by solving the following optimization problem

$$\min_{\boldsymbol{x}_2} \sum_{p} W_p \left(|\ \widehat{H}_{p,th}(\boldsymbol{x}_1, \boldsymbol{x}_2)\ | - |\ \widehat{H}_{p,exp}\ | \right)^2 \quad \text{with } p = u_I, \ddot{u}_I^{(tot)}, u_{TI}, \ddot{u}_T^{(tot)}, F_B \tag{14}$$

seeking to minimize the sum of the squared differences between experimentally and numerically obtained FRFs in terms of primary mass displacement relative to the ground, primary mass total acceleration, relative displacement between primary and secondary mass (i.e., TMDI stroke), secondary mass total acceleration, and inerter force. In the last equation, $W_p = 1/\max\left(\left|\widehat{H}_{p,exp}\right|\right)$ and $H_{p,exp}$ are the experimentally determined FRFs of the p-th response quantity obtained by sine sweep excitation with PGA = 0.10 g applied to the considered reference physical system. Further, $H_{p,th}$ are FRFs numerically determined by solving (i.e., numerically integrating) Eqs.(12) for the same sine sweep excitation. The optimization problem in Eq.(14) is solved numerically using a standard least-

square minimization algorithm implemented in the built-in MATLAB® routine '*lsqnonlin*' and the following results have been obtained$k_{1I} = 3.94 \times 10^4\ N/m$, $k_{2I} = -6.46 \times 10^5\ N/m^2$, $k_{3I} = 4.52 \times 10^6\ N/m^3$, $c_I = 538.13\ Ns/m$, $k_{1T} = 5.55 \times 10^4\ N/m$, $k_{2T} = -1.15 \times 10^6\ N/m^2$, $k_{3T} = 8.48 \times 10^6\ N/m^3$ and $c_T = 409.15\ Ns/m$.

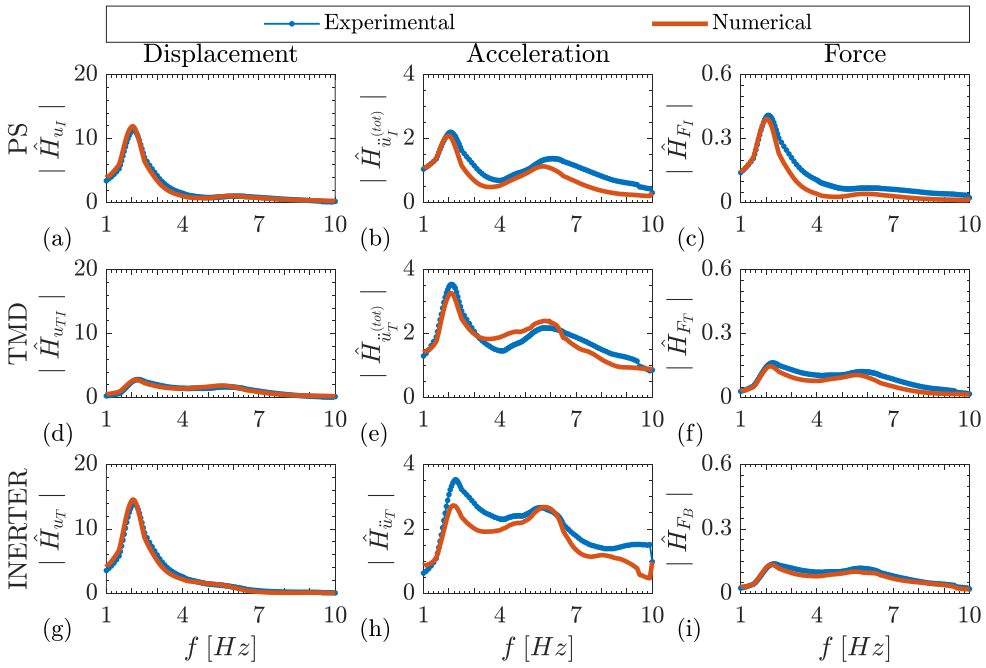

Figure 17. Comparison of experimental FRFs with numerical FRFs with nonlinear inerter of (a) primary mass displacement, (b) primary mass acceleration, (c) primary isolator shearing force, (d) TMDI stroke, (e) secondary mass acceleration, (f) secondary isolator shearing force, (g) secondary mass displacement, (h) inerter relative acceleration, and (i) inerter force of TMDI controlled PS with mass ratio μ=0.080 and various inertance ratios under sine-sweep excitation with *PGA*=0.10g.

The experimental and numerical FRFs are compared in Figure 17. Close point-wise matching is observed across all frequencies for displacement responses (first column of panels in Figure 17), while good matching is observed for force FRFs and acceleration FRF response of the primary and secondary mass within the critical frequency ranges around the two system resonant frequencies. These observations give confidence to the quality of the undertaken experimental campaign and to the validity of the measured data presented in Section 3 and their interpretation and, at the same time,

demonstrate the appropriateness of the parametric nonlinear model in Eq. (12) to capture faithfully the salient response features of PS and the secondary mass of the physical models.

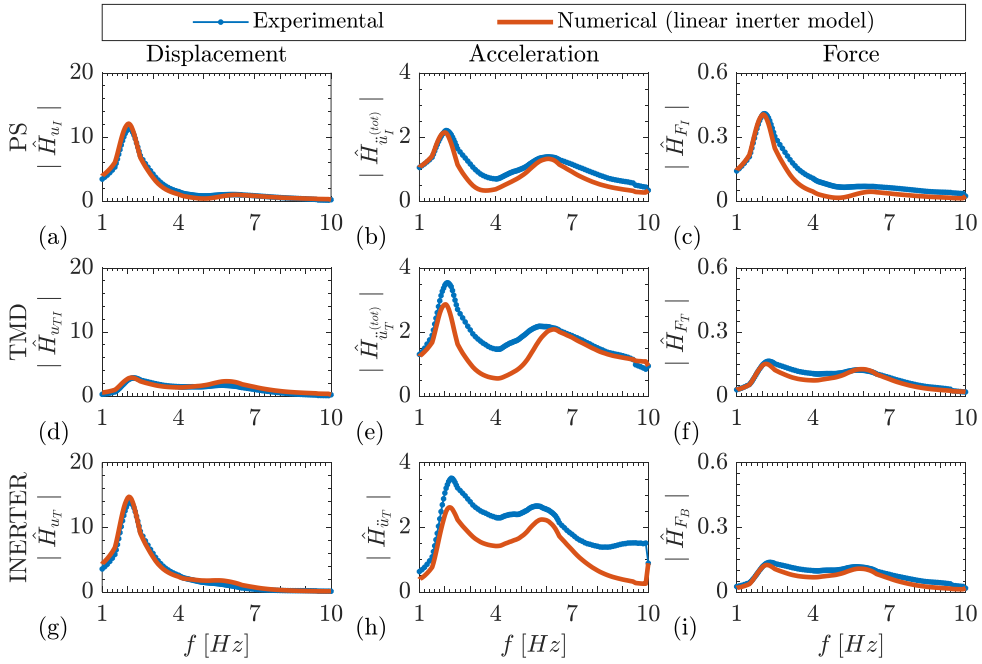

Figure 18. Comparison of experimental FRFs with numerical FRFs with linear inerter model of (a) primary mass displacement, (b) primary mass acceleration, (c) primary isolator shearing force, (d) TMDI stroke, (e) secondary mass acceleration, (f) secondary isolator shearing force, (g) secondary mass displacement, (h) inerter relative acceleration, and (i) inerter force of TMDI controlled PS with mass ratio μ=0.080 and various inertance ratios under sine-sweep excitation with *PGA*=0.10g.

The latter consideration provides the opportunity to examine in a direct manner the effect of the adopted inerter device, which deviates from the ideal inerter element adopted by previous theoretical studies [13, 28-30, 49], to the response of nonlinear structures. This is pursued by considering a variant nonlinear numerical model in which the nonlinear inerter mechanical model of Figure 16 is replaced by a linear (ideal) inerter element with nominal inertance of 48.7kg corresponding to the specimen with intermediate inertance. The previously derived nonlinear elastic stiffness HDRB properties are maintained while the equivalent damping property of the HDRBs are updated as $c_I = 743.3\ Ns/m$ and $c_T = 324.7\ Ns/m$ derived by solving the optimization problem in Eq.(14) for the variant numerical model. Numerical FRFs for the variant nonlinear model with ideal

inerter are compared in Figure 18 with previous experimental FRFs. It is seen that the assumption of an ideal inerter deteriorates the model capability to capture acceleration FRFs for the secondary mass and the inerter (see Figures 18(e,h) vis-à-vis 17(e,h)). Hence, deviation from the ideal inerter behavior influences nonlinear TMDI acceleration kinematics and should be accounted for in TMDI assessment. However, FRFs of the variant nonlinear model with ideal inerter achieves excellent matching of the experimental the PS FRFs (first row of panels in Figure 18) at the first resonant frequencies. This outcome signifies that nonlinear inerter device behavior does not affect much the response of nonlinear TMDI-equipped structures. Therefore, the assumption of modelling the inerter device as a linear ideal inerter element with some representative (nominal) inertance suffices in undertaking optimal TMDI design/tuning to minimise PS response. This is a practically important consideration as it allows for simplified optimal TMDI tuning approaches for harmonic excitations assuming ideal inerter behavior such as the one considered in [49] and extends their range of applicability to the case of nonlinear structures.

5. Concluding remarks

A novel shaking table testing campaign was undertaken to study the response of TMDI-equipped SDOF PSs under harmonic base-excitation accounting for the combined effects of nonlinear structural behaviour, exhibited by the HDRBs of the PS and the TMDI, and of deviation from the ideal linear inerter element behaviour, exhibited by the custom-built grounded rack-and-pinion flywheel inerter device. Comprehensive experimental data in time and frequency domains were presented pertaining to a parametric experimental investigation involving 9 specimens with different combination of TMDI inertial properties (secondary mass and inertance) subject to sine sweep excitations for three different amplitudes. Stronger nonlinear elastic behaviour of the softening kind with increasing excitation amplitude was verified for the HDRBs in all the specimens by noting changes to the resonant structural frequencies as well as by inspecting experimental force-

deformation curves at resonant frequencies and steady-state conditions. Further, the reported experimental force-relative acceleration and force-deformation curves for the inerter device exhibited significant deviation from the ideal inerter element attributed to friction and gears play/backlash effects, although, on average, the nominal inertance has been verified. Yet, irrespective of the level of nonlinear structural behaviour and deviation from the ideal inerter, the provided experimental data verified the same TMDI motion control attributes found in previous theoretical studies assuming linear structural behaviour and ideal inerter element [13, 28, 49]. These are: (i) the TMDI becomes more effective in mitigating simultaneously PS displacement, acceleration and base shear response as well as secondary mass stroke with increasing inertance and fixed secondary mass, and (ii) the positive TMDI motion control effect of PS response with increasing secondary mass saturates and, eventually, becomes insignificant with increasing inertance. In this respect, the significant practical advantage of the TMDI over TMD of overall improved vibration suppression through increasing inertance rather than increasing secondary mass/weight leading to lightweight vibration absorbers extends to the case of nonlinear structures and inerter devices. More importantly, the comparison of experimental FRFs with FRFs derived from two nonlinear parametric numerical models capturing faithfully the nonlinear response of the HDRBs, one adopting a nonlinear mechanical model to represent the inerter device and the other an ideal linear inerter element, has demonstrated that PS nonlinear response is insignificantly influenced by the deviation of the inerter device from the ideal inerter element. This outcome suggests that adopting the ideal inerter assumption does not compromise the accuracy of simplified, thus practically meritorious, optimal TMDI tuning approaches as the one in [49]. Still, the above major conclusions and practical recommendations have only been herein demonstrated for harmonic excitations. In this respect, further experimental research is warranted to address the case of non-harmonic and transient excitations in order to establish the efficacy of TMDI with grounded inerter to protect nonlinear/yielding structures subject to earthquake

induced excitations as well as to study the response of TMDI with non-grounded inerter applicable to placement within multi-DOF structural systems.

Acknowledgements

The financial support of Sapienza University of Rome under the Grant No. RM11715C8262BE71 (financial framework 2017), is gratefully acknowledged.

References

[1] B.F. Spencer Jr, S. Nagarajaiah, State of the art of structural control, Journal of structural engineering, 129(7) (2003) 845-856.

[2] T.T. Soong, B.F. Spencer Jr, Supplemental energy dissipation: state-of-the-art and state-of-the-practice, Engineering Structures, 24(3) (2002) 243-259.

[3] J.C. Simo, J.M. Kelly, The Analysis of Multilayer Elastomeric Bearings, ASME Journal of Applied Mechanics 51(2) (1984) 256–262. https://doi.org/10.1115/1.3167609.

[4] P.S. Harvey Jr, C.K. Kelly, A review of rolling-type seismic isolation: Historical development and future directions, Engineering Structures 125 (2016) 521-531.

[5] Elias, S. and Matsagar, V. (2017). "Research developments in vibration control of structures using passive tuned mass dampers." Annual Reviews in Control, 44: 129-156.

[6] J.P. Den Hartog, Mechanical Vibrations, 4th ed, McGraw-Hill, New York, 1956.

[7] S. Elias, V. Matsagar, T.K. Datta (2019) Distributed Tuned Mass Dampers for Multi-Mode Control of Benchmark Building under Seismic Excitations, Journal of Earthquake Engineering, 23 (2019) 1137-1172.

[8] Y. Hu, M. Z.Q. Chen. Performance evaluation for inerter-based dynamic vibration absorbers, International Journal of Mechanical Sciences 99 (2015) 297-307.

[9] X. Jin, M. Z. Q. Chen, Z. Huang, Minimization of the beam response using inerter-based passive vibration control configurations, International Journal of Mechanical Sciences 119 (2016) 80-87.

[10] E. Barredo, A. Blanco, J. Colín, V.M. Penagos, A. Abúndez, L.G. Vela, …, J. Mayén, Closed-form solutions for the optimal design of inerter-based dynamic vibration absorbers, International Journal of Mechanical Sciences 144 (2018) 41-53.

[11] K. Ikago, K. Saito, N. Inoue, Seismic control of single-degree-of-freedom structure using tuned viscous mass damper, Earthquake Engineering & Structural Dynamics 41(3) (2012) 453-474.

[12] I.F. Lazar, S.A. Neild, D.J. Wagg, Using an inerter-based device for structural vibration suppression, Earthquake Engineering and Structural Dynamics 43(8) (2012) 1129–1147.

[13] L. Marian, A. Giaralis, Optimal design of a novel tuned mass-damper-inerter (TMDI) passive vibration control configuration for stochastically support-excited structural systems, Probabilistic Engineering Mechanics 38 (2014) 156–164.

[14] M.C. Smith, Synthesis of mechanical networks: the inerter, IEEE Transactions on Automatic Control 47(10) (2002) 1648–1662.

[15] S. Krenk, J. Høgsberg, Tuned resonant mass or inerter-based absorbers: unified calibration with quasi-dynamic flexibility and inertia correction, Proceedings of the Royal Society A: Mathematical, Physical and Engineering Sciences 472(2185) (2016) 20150718.

[16] Y. Wen, Z. Chen, X. Hua, Design and Evaluation of Tuned Inerter-Based Dampers for the Seismic Control of MDOF Structures, Journal of Structural Engineering 143(4) (2017) 04016207.

[17] D. Pietrosanti, M. De Angelis, M. Basili, Optimal design and performance evaluation of systems with Tuned Mass Damper Inerter (TMDI), Earthquake Engineering and Structural Dynamics 46(8) (2017) 1367–1388. https://doi.org/10.1002/eqe.2861.

[18] S.Y. Zhang, J.Z. Jiang, S. Neild, Optimal configurations for a linear vibration suppression device in a multi-storey building, Structural Control and Health Monitoring 24(3) (2017) e1887.

[19] A. Giaralis, F. Petrini, Wind-induced vibration mitigation in tall buildings using the tuned mass-damper-inerter, Journal of Structural Engineering 143 (2017) 04017127.

[20] F. Petrini, A. Giaralis, Z. Wang. Optimal tuned mass-damper-inerter (TMDI) design in wind-excited tall buildings for occupants' comfort serviceability performance and energy harvesting. *Engineering Structures*, 204 (2020) 109904.

[21] A. Giaralis, A. Taflanidis, Optimal tuned mass-damper-inerter (TMDI) design for seismically excited MDOF structures with model uncertainties based on reliability criteria, Structural Control and Health Monitoring 25(2) (2018) e2082.

[22] R. Ruiz, A.A. Taflanidis, A. Giaralis, D. Lopez-Garcia, Risk-informed optimization of the tuned mass-damper-inerter (TMDI) for the seismic protection of multi-storey building structures, Engineering Structures 177 (2018) 836-850.

[23] C. Pan, R.F. Zhang, Design of structure with inerter system based on stochastic response mitigation ratio, Structural Control and Health Monitoring (2018) 25(6): e2169. http://doi.org/10.1002/stc.2169.

[24] A.A. Taflanidis, A. Giaralis, D. Patsialis, Multi-objective optimal design of inerter-based vibration absorbers for earthquake protection of multi-storey building structures, Journal of the Franklin Institute 356(14) (2019) 7754-7784.

[25] Z.P. Zhao, R.F. Zhang, Y.Y. Jiang, C. Pan, A tuned liquid inerter system for vibration control, International Journal of Mechanical Sciences, (2019) 164: 105171. https://doi.org/10.1016/j.ijmecsci.2019.105171.

[26] M. Saitoh, On the performance of gyro-mass devices for displacement mitigation in base isolation systems, Structural Control and Health Monitoring 19(2) (2012) 246–259.

[27] C. Zhao, J. Kikuchi, M. Ikenaga, K. Ikago, N. Inoue, Viscoelastically supported viscous mass damper incorporated into a seismic isolation system, Journal of Earthquake and Tsunami 10(3) (2016) 1640009.

[28] D. De Domenico, G. Ricciardi, An enhanced base isolation system equipped with optimal tuned mass damper inerter (TMDI), Earthquake Engineering and Structural Dynamics 47 (2018) 1169-1192.

[29] D. De Domenico, G. Ricciardi, Optimal design and seismic performance of tuned mass damper inerter (TMDI) for structures with nonlinear base isolation systems, Earthquake Engineering and Structural Dynamics 47 (2018) 2539-2560.

[30] M. De Angelis, A. Giaralis, F. Petrini, D. Pietrosanti, Optimal tuning and assessment of inertial dampers with grounded inerter for vibration control of seismically excited base-isolated systems, Engineering Structures 196 (2019) 109250. https://doi.org/10.1016/j.engstruct.2019.05.091.

[31] M. Basili, M. De Angelis, D. Pietrosanti, Dynamic response of a viscously damped two adjacent degree of freedom system linked by inerter subjected to base harmonic excitation,

Procedia Engineering 199 (2017) 1586–1591. https://doi.org/10.1016/j.proeng.2017.09.062.

[32] M. Basili, M. De Angelis, D Pietrosanti, Modal analysis and dynamic response of a two adjacent single degree of freedom systems linked by spring-dashpot-inerter elements, Engineering Structures 174 (2018) 736-752. https://doi.org/10.1016/j.engstruct.2018.07.048.

[33] M. Basili, M. De Angelis, D. Pietrosanti, Defective two adjacent single degree of freedom systems linked by spring-dashpot-inerter for vibration control, Engineering Structures 188 (2019) 480-492. https://doi.org/10.1016/j.engstruct.2019.03.030.

[34] C. Papageorgiou, N.E. Houghton, M.C. Smith, Experimental testing and analysis of inerter devices, Journal of Dynamic Systems, Measurement and Control 131(1) (2008) 011001. https://doi.org/10.1115/1.3023120.

[35] R.M. Hessabi, O. Mercan, Investigations of the application of gyro-mass dampers with various types of supplemental dampers for vibration control of building structures, Engineering Structures 126 (2016) 174-186.

[36] P. Brzeski, M. Lazarek, P. Perlikowski, Experimental study of the novel tuned mass damper with inerter which enables changes of inertance, Journal of Sound and Vibration 404 (2017) 47–57.

[37] K. Saito, Y. Sugimura, S. Nakaminami, H. Kida, N. Inoue, Vibration tests of 1-story response control system using inertial mass and optimized soft spring and viscous element, 14th World Conference on Earthquake Engineering, Beijing, China, 2008, 12-01.

[38] Y. Watanabe, K. Ikago, N. Inoue, H. Kida, S. Nakaminami, H. Tanaka, Y. Sugimura, K. Saito, Full-scale dynamic tests and analytical verification of a force-restricted tuned viscous mass damper, 15th World Conference on Earthquake Engineering. Lisbon, Portugal, 2012.

[39] Y. Nakamura, A. Fukukita, K. Tamura, I. Yamazaki, T. Matsuoka, K. Hiramoto, K. Sunakoda, Seismic response control using electromagnetic inertial mass dampers, Earthquake Engineering & Structural Dynamics 43(4) (2014) 507-527.

[40] H. Zhu, Y. Li, W. Sehn, S. Zhu, Mechanical and energy-harvesting model for electromagnetic inertial mass dampers, Mechanical Systems and Signal Processing 120 (2019) 203-220.

[41] S.J. Swift, M.C. Malcolm, A.R. Glover, C. Papageorgiou, B. Gartner, H.E. Neil, Design and modelling of a fluid inerter, International Journal of Control 86(11) (2013) 2035–2051.

[42] S. Kawamata, Development of a vibration control system of structures by means of mass pumps, in, Institute of Industrial Science, University of Tokyo, 1973.

[43] X. Liu, J.Z. Jiang, B. Titurus, A. Harrison, Model identification methodology for fluid-based inerters, Mechanical Systems and Signal Processing 106 (2018) 479-494.

[44] F.C. Wang, M.F. Hong, T.C. Lin, Designing and testing a hydraulic inerter, Proceedings of the Institution of Mechanical Engineers, Part C: Journal of Mechanical Engineering Science 225(1) (2011) 66-72.

[45] S. Nakaminami, H. Kida, K. Ikago, N. Inoue, Dynamic testing of a full-scale hydraulic inerter-damper for the seismic protection of civil structures, 7th International conference on advances in experimental structural engineering, 2016, 41-54. https://doi.org/10.7414/7aese.T1.55. 2016.

[46] P. Brzeski, P. Perlikowski, Effects of play and inerter nonlinearities on the performance of tuned mass damper, Nonlinear Dynamics 88 (2017) 1027–1041.

[47] D. De Domenico, P. Deastra, G. Ricciardi, N.D. Sims, D.J. Wagg, Novel fluid inerter based tuned mass dampers for optimised structural control of base-isolated buildings, Journal of the Franklin Institute, 2018.

[48] A. Gonzalez-Buelga, I.F. Lazar, J.Z. Jiang, S.A. Neild, D.J. Inman, Assessing the effect of nonlinearities on the performance of a tuned inerter damper, Structural Control and Health Monitoring 24(3) (2017) e1879.

[49] L. Marian, A. Giaralis, The tuned mass-damper-inerter for harmonic vibrations suppression, attached mass reduction, and energy harvesting, Smart Structures and Systems 19(6) (2017) 665–678.

[50] F. Naeim, J. Kelly, Design of Seismic Isolated Structures: From Theory to Practice, Wiley, New York (1999).

[51] A.A. Markou, G.D. Manolis, Mechanical models for shear behavior in high damping rubber bearings, Soil Dynamics and Earhtquake Engineering¬ 90 (2016) 221-226.

[52] D. Pietrosanti, Study of Inerter as innovative device in vibration control, Ph.D. Thesis, Sapienza University of Rome, 2019.

[53] F. Scheibe, M.C. Smith, A behavioral approach to play in mechanical networks, SIAM Journal of Control Optimization 47(6) (2009) 2967–2990.